Diabatic Rossby Vortex World: Finite Amplitude Effects in Moist Cyclogenesis

Matthieu Kohl and Paul A. O'Gorman

Department of Earth, Atmospheric, and Planetary Sciences, Massachusetts Institute of Technology, Cambridge, Massachusetts

Corresponding author: Matthieu Kohl, mkohl@mit.edu

ABSTRACT: Diabatic Rossby Vortices (DRVs) are a special class of heavily precipitating extratropical cyclone in which latent heating effects play a key role. As such their dynamics defies the classic mechanism of midlatitude storm formation and poses challenges to modelling and theoretical understanding. Here we build on recent theoretical advances on the growth of DRV modes in small-amplitude moist instability calculations by exploring the structure of finite-amplitude DRV storms in a hierarchy of models of moist macroturbulence. Simulations of moist quasigeostrophic turbulence show a transition to a DRV dominated flow (DRV world) when the latent heating is strong. The potential vorticity (PV) structure of the DRVs is similar to the PV structure from small-amplitude DRV modal theory. Simulations of the moist primitive equations also transition to DRV world when both the latent heating is strong and the Rossby number is sufficiently low. At high Rossby numbers, however, the PV structure of storms with strong latent heating is bottom-intensified compared to DRV modal theory due to higher order effects beyond quasigeostrophy, and the macroturbulent flow has both DRV-like storms and frontal structures. A 1-D model of the vertical structure of PV is solved for different Rossby numbers and stratification profiles to reconcile the PV structures of DRVs in the simulations, small-amplitude modal theory, and observations.

SIGNIFICANCE STATEMENT: Diabatic Rossby Vortices (DRVs) are a special class of heavily precipitating extratropical cyclones which grow from the effects of latent heating and as such go beyond the classic growth mechanism of midlatitude storm formation. DRVs have been implicated in extreme and poorly predicted forms of cyclogenesis and pose challenges to both modeling and theoretical understanding. Here, we extend our previous study on the structure and emergence of DRVs in small-amplitude instability calculations by exploring the structure of DRV storms and the conditions for the emergence of DRV dominated atmospheres ('DRV world') in a range of different finite-amplitude simulations.

1. Introduction

Past research has identified a special class of midlatitude storm, dubbed the Diabatic Rossby Vortex (DRV) (also referred to as Diabatic Rossby Wave), which derives its energy from the release of latent heat associated with condensation of water vapor, and as such differs fundamentally from the traditional understanding of midlatitude storm formation (Wernli et al. 2002; Moore and Montgomery 2004, 2005; Moore et al. 2008). DRVs have been found to be involved in the development of extreme and poorly predicted storms along the east coast of the US and the west coast of Europe with significant damage to property and human life (Wernli et al. 2002; Boettcher and Wernli 2013; Moore et al. 2008). DRVs have been identified in all oceans basins and seasons, and occur at a rate of roughly 10 systems per month in the Northern Hemisphere and 4 systems per month in the Southern Hemisphere (Boettcher and Wernli 2013, 2015).

More recently, moist baroclinic instability calculations with an idealized GCM over a wide range of climates have shown that DRVs become the dominant mode of moist baroclinic instability in sufficiently warm climates, pointing to the increased role DRVs might play in the development of fast growing disturbances in a warming climate (O'Gorman et al. 2018). While we have a good theoretical understanding of classic cyclogenesis, both in terms of simple conceptual models of baroclinic instability (Eady 1949; Charney 1947; Phillips 1954; Emanuel et al. 1987; Fantini 1995; Zurita-Gotor 2005) and potential vorticity (PV) dynamics of finite-amplitude storms (Davis and Emanuel 1991), we have less understanding of the formation and propagation of DRVs, the controls on their growth rates and length scales, and their response under climate change. Given the importance of diabatic effects in cyclogenesis in the current climate and more so in a warming climate, developing an equivalent theoretical understanding for DRVs is critical.

In a recent paper, we isolated the DRV growth mechanism within a conceptually simple and analytically tractable model and used it to derive theoretical results for the growth rate and length scale of such disturbances (Kohl and O'Gorman 2022). The model was a moist two-layer quasi-geostrophic (QG) system in which the effects of latent heating were represented through a reduction of the static stability in updrafts in the spirit of simple moist baroclinic theories (Emanuel et al. 1987). The boundaries were tilted at a variable slope relative to the mean isentrope, thereby allowing us to control the strength of meridional PV advection relative to diabatic generation from latent heating. In particular this allowed us to study a pure latent-heating driven disturbance with no meridional PV advection. We showed that DRVs emerge as the fastest growing modes of moist baroclinic instability when the meridional PV gradients are weak and the moist static stability is also sufficiently weak (i.e., the latent heating is sufficiently strong). Furthermore, we developed a simple PV argument to explain the transition from wave to vortex modes observed in idealized GCM simulations of warm climates (O'Gorman et al. 2018). Finally, analytical solutions were derived for a DRV mode in an unbounded domain, and a threshold of $r = 0.38$ was found above which DRV solutions cease to exist, where r is the factor by which the static stability is reduced by latent heating in rising air.

While the two-layer QG results in Kohl and O'Gorman (2022) makes progress on the growth mechanism and PV structure of DRV modes, they are based around an assumption of small amplitude disturbances, and the implications for finite amplitude disturbances require further investigation. Comparing the structure of DRV modes to DRV storms in current and future climates, for instance, we showed that finite amplitude effects (e.g., vertical PV advection, ageostrophic advection) must be taken into account to relate the structure of PV anomaly and diabatic generation in certain observed storms (Kohl and O'Gorman 2022). Furthermore, the small-amplitude instability results from the idealized GCM show that the fastest growing mode transitions to a DRV rather than a wave in warm climates, but the corresponding macroturbulent state in the idealized GCM remains wavy and is not dominated by DRVs (O'Gorman et al. 2018), even if DRVs can be identified (Kohl and O'Gorman 2022). It remains unclear if a macroturbulent flow at statistical equilibrium with strong latent heating can transition to a completely DRV dominated flow, which we will refer to as a 'DRV world' from here on.

The goal of this paper is to go beyond small-amplitude DRV modes and study the dynamics of finite amplitude DRVs and the potential for a transition to DRV world in a hierarchy of different models of moist macroturbulence, including simulations of moist macroturbulence using the QG equations, simulations of moist macroturbulence using the primitive equations, and a simple 1D model for the vertical structure of PV in small-amplitude DRV modes vs. finite-amplitude storms. Previous studies of the effects of moisture on macroturbulence in simple models have illustrated the ways in which latent heating influences the flow (Lapeyre and Held 2004; Lambaerts et al. 2011, 2012; Brown et al. 2023; Bembenek et al. 2020; Lutsko et al. 2024). In particular, the pioneering study of Lapeyre and Held (2004) using a two-layer QG model found a transition to a vortex dominated flow for sufficiently strong latent heating. While it is possible to include a moisture equation and even simple precipitation physics in a QG framework (Smith and Stechmann 2017), the spirit of our simulations is to keep the representation of moist physics as simple as possible by sticking to the reduced stability parameterization of latent heating from modal theory (Emanuel et al. 1987, Fantini 1995, Kohl and O'Gorman 2022). Using this simple representation of latent heating allows a direct comparison with small-amplitude modal theory as we gradually introduce higher order terms in the dynamics. Our approach is deliberately phenomenological, studying large parameter ranges in a range of different models so as to explore the conditions leading to a clear transition to DRV world and to explore the differences between the behavior of small-amplitude modes and finite amplitude storms.

In section 2, we begin by analyzing simulations of moist QG turbulence as a natural extension of the 2-layer moist QG theory of DRV modes presented in Kohl and O'Gorman (2022). The QG simulations parallel previous two-layer studies using a prognostic moisture equation (Lapeyre and Held 2004; Bembenek et al. 2020; Brown et al. 2023; Lutsko et al. 2024), but with the reduced stability parameterization for latent heating (Emanuel et al. 1987) which greatly reduces the number of parameters involved and allows for better comparison with the work of O'Gorman et al. (2018) and Kohl and O'Gorman (2022). We show that the flow transitions from a state of wavy jets interspersed with vortices to a vortex dominated flow ('DRV world') as the latent heating is increased. By analyzing the PV structure and PV budget of the storms in the strong latent heating regime of the QG simulations, we confirm that the flow has transitioned to DRV world. In section 3, we study moist primitive equation simulations in low, intermediate and high Rossby number regimes to explore the effects of higher-order effects beyond QG on the structure of diabatically driven storms and the overall character of the macroturbulent circulation. The simulations are an attempt to bridge the gap between theoretical studies of DRVs based around the moist-QG equations versus GCM simulations and observations. In particular, strong latent heating is found to lead to a DRV world at low Rossby number but not at high Rossby number. In section 4, we distill higher-order effects into a toy model of the vertical structure of PV in DRVs that is solved to reproduce much of the variety of the PV structure of DRV storms from the simulations in the previous two sections of the paper and also from reanalysis (Kohl and O'Gorman 2022). In section 5, we summarize our results and discuss future work.

2. DRVs in Simulations of Moist QG Turbulence

a. Model Formulation and Governing Equations

A natural extension of the two-layer moist QG theory of DRV modes presented in Kohl and O'Gorman (2022) is to run simulations of moist QG turbulence. The two-layer moist QG equations with equal layer height, β-plane approximation and low level drag take the nondimensional form

$$\partial_t \nabla^2 \phi + J(\phi, \nabla^2 \phi) + J(\tau, \nabla^2 \tau) + \beta \phi_x = -\frac{R}{2} \nabla^2 (\phi - \tau), \tag{1}$$

$$\partial_t \nabla^2 \tau + J(\phi, \nabla^2 \tau) + J(\tau, \nabla^2 \phi) + \beta \tau_x + w = \frac{R}{2} \nabla^2 (\phi - \tau), \tag{2}$$

$$\partial_t \tau + J(\phi, \tau) + r(w) w = \overline{r(w) w}, \tag{3}$$

with barotropic and baroclinic stream function $\phi = \frac{\psi_1 + \psi_2}{2}$ and $\tau = \frac{\psi_1 - \psi_2}{2}$ where ψ_1 refers to the streamfunction in the upper layer and ψ_2 to the streamfunction in the lower layer, and with Jacobian $J(A, B) = A_x B_y - A_y B_x$ and domain mean average $\overline{(\ldots)}$ where subscripts are used to denote partial derivatives. The equations have been nondimensionalized assuming an advective time scale, with the deformation radius $L_D = NH/(\sqrt{2} f)$ as the length scale, where H is the layer height, and U as the velocity scale which is equivalent to the zonal velocity in the basic static described below (U

in the top layer, and $-U$ in the bottom layer).[1] Non-dimensional numbers include $R = R_{dim} L_D / U$ where R_{dim} is the dimensional drag coefficient, and $\beta = \beta_{dim} L_D^2 / U$ where β_{dim} is the dimensional β parameter. Effects of latent heating on the dynamics are encapsulated in the spirit of simple moist theories (Emanuel et al. 1987; Fantini 1995) by the nonlinear factor

$$r(w) = \begin{cases} r, & w \geq 0 \\ 1, & w < 0 \end{cases} \tag{4}$$

which reduces the static stability by a factor r in regions of ascent. Physically, the nonlinear factor $r(w)$ captures that as moist air ascends, it releases latent heat through condensation, resulting in a locally reduced static stability. Conversely, descending air, having undergone precipitation and become subsaturated, experiences the full static stability. Moist thermodynamics thus introduces an additional nonlinearity into the equations which can lead to interesting dynamics. We keep $r > 0$ so that there is no convective instability. The term $\overline{r(w)w}$ in Eq. 3 acts as a spatially uniform radiative cooling to ensure that the domain-mean temperature remains constant even though there is latent heating. Eqs. (1-3) are obtained from Eqs. A6-A8 in Kohl and O'Gorman (2022) after setting the boundaries at top and bottom to be horizontal $h_1 = h_2 = 0$, and including the β effect and low level drag.

The system is allowed to go moist baroclinically unstable about a mean temperature gradient in thermal wind balance, which corresponds to $\tau_0 = -y$, $\phi_0 = 0$ and $w_0 = 0$. We set $\tau = \tau_0 + \tau'$, $\phi = \phi'$, and $w = w'$. Eqs. (1-3) then take the form

$$\partial_t \nabla^2 \phi + J(\phi, \nabla^2 \phi) + J(\tau, \nabla^2 \tau) + \beta \phi_x = -\nabla^2 \tau_x - \frac{R}{2} \nabla^2 (\phi - \tau) - \mu \nabla^4 (\nabla^2 \phi), \tag{5}$$

$$\partial_t \nabla^2 \tau + J(\phi, \nabla^2 \tau) + J(\tau, \nabla^2 \phi) + w + \beta \tau_x = -\nabla^2 \phi_x + \frac{R}{2} \nabla^2 (\phi - \tau) - \mu \nabla^4 (\nabla^2 \tau), \tag{6}$$

$$\partial_t \tau + J(\phi, \tau) + r(w) w = \phi_x - \mu \nabla^4 \tau - \alpha \tau + \overline{r(w) w} \tag{7}$$

where we have dropped all the primes for notational simplicity, and ϕ, τ and w represent perturbations about the basic state that have spatially homogeneous statistics. The horizontal means of the stream functions ϕ and τ, and the mean of w are all enforced to be zero. Setting the mean

[1] Discretizing the continous thermodynamic equation leads to a deformation radius involving N, rather than a reduced gravity, at the mid-tropospheric level.

of τ to zero is equivalent to including the spatially uniform radiative cooling term $\overline{r(w)w}$. Eqs. (5-7) also include a small-scale dissipation parametrized by a fourth-order hyper-diffusion with coefficient μ; and a large-scale radiative damping parameterized by a linear Newtonian relaxation with coefficient α. The large-scale radiative damping was found to be necessary for simulations with roughly $r < 0.4$ and thus large energy input from latent heating because the linear drag term was not enough to remove the energy at large scales and allow the simulations to reach a statistical steady state (see section 2d for further details). The inability of the static stability to adjust in QG and the imposition of a fixed meridional temperature gradient make for a particularly simple and homogeneous model setup for analysis, but they also tend to limit the ability of the QG model to equilibrate.

Our system of moist QG equations differs from those of Lapeyre and Held (2004), Brown et al. (2023), and Lutsko et al. (2024) primarily by always assuming upward motion to be saturated. Thus, no prognostic moisture equation is needed, and the effects of latent heating are captured in terms of a single parameter r. So far the r parametrization has been used in studies of moist baroclinic instability as an initial value problem (Emanuel et al. 1987, Montgomery and Farrell 1991, Montgomery and Farrell 1992, Fantini 1995, Moore and Montgomery 2004, Kohl and O'Gorman 2022) with the exception of O'Gorman et al. (2018) which considered both small-amplitude instability and a macroturbulent steady state. To our knowledge, this is the first time that the r-parametrization has been applied to macroturbulent simulations in a two-layer model. We choose this system here for its simplicity and ease of comparison to moist baroclinic theories, but acknowledge that having a prognostic moisture equation, like in Lapeyre and Held (2004), allows for conservation properties that are more desirable when developing closure theories for PV fluxes (which is not our focus here). A comparison of our simulations to previous studies using a prognostic moisture equation is given in Appendix A.

b. Numerical Simulations: Dry vs. Moist Regimes

We solve the moist two-layer QG Eqs. (5-7) on a doubly-periodic domain of size $L = 12\pi$ with 512x512 grid points using Dedalus, a flexible framework for numerical simulations with spectral methods (Burns et al. 2020). Dedalus advances the entire state forward in time simultaneously using a mixed implicit-explicit scheme, implicitly solving the time updates and other linear terms, and thus it is not a problem that both Eqs. 6 and 7 involve time derivatives of τ. The nonlinear dependence of latent heating on the vertical velocity through $r(w)$ means that the equations are highly nonlinear, and it would be difficult to prove the solutions are unique. However, our previous results from solving a nonlinear QG omega equation with this representation of latent heating were in good agreement with solutions of the primitive equations (see Figure 1 of Kohl and O'Gorman (2024)).

We show results for simulations with $r = 1$ (a dry simulation) and $r = 0.01$ (a moist simulation with strong latent heating). We fix $\beta = 0.78$ equal to the value of Lapeyre and Held (2004).[2] This corresponds to a moderate dry supercriticality of $\chi = \beta^{-1} = 1.28$, where $\chi > 1$ is required for the inviscid dry model to go unstable. We set $R = 0.11$ and $\mu = 10^{-5}$ for both values of r. We set $\alpha = 0$ for $r = 1$ and $\alpha = 1.7$ for $r = 0.01$. The simulations are started using random initial conditions for the stream functions ϕ and τ, where we have filtered out all wavenumbers with $k = \sqrt{k_x^2 + k_y^2} > 3$ to avoid having to integrate a lot of small scale noise in the initial phase of the simulation. The simulations are run from $t = 0$ until $t = 120$ at $r = 0.01$ and $t = 150$ at $r = 1$ and outputted in snapshots at time intervals of 0.25. After an initial phase of modal instability, the simulations settle into a macroturbulent state (roughly at $t = 40$ for $r = 0.01$ and $t = 60$ at $r = 1$). This happens more quickly at $r = 0.01$ because the growth rate of the modes is increased by latent heating.

We begin by comparing the structure of the flow field in the two simulations. The relative vorticity in the upper and lower layer, alongside the vertical velocity are shown in Fig. 1. Looking at the dry simulation (Fig. 1a,c,e), we see that the flow settles into the well known state of β-plane turbulence: wavy jets interspersed with vortices. The relative vorticity is weaker in the lower than upper layer because of the low level drag. The vertical velocity field has large-scale ascending and descending regions of similar area and magnitude that are mostly confined to the latitude bands of the jets. We have provided an animation in Supplemental Video S1.

In contrast to the dry simulation, we see that the flow in the moist simulation at $r = 0.01$ (Fig. 1 b, d, f) has transitioned to a DRV world that is dominated by small scale vortices, despite the presence of β. In fact when the simulation was run with β changed down to $\beta = 0$ or up to $\beta = 1.5$, there was no noticeable effect on the overall flow field (not shown). As explored in the next section, tendencies in the PV budget at this low $r = 0.01$ are dominated by diabatic generation, nonlinear advection and

[2]Please note that compared to Lapeyre and Held (2004), our deformation radius is defined as $L_D = NH/(\sqrt{2}f)$ instead of $L_D = NH/f$ but the magnitude of our mean flow is U instead of their $U/2$ so that the definition of $\beta = \beta_{dim} L_D^2/U$ is equivalent.

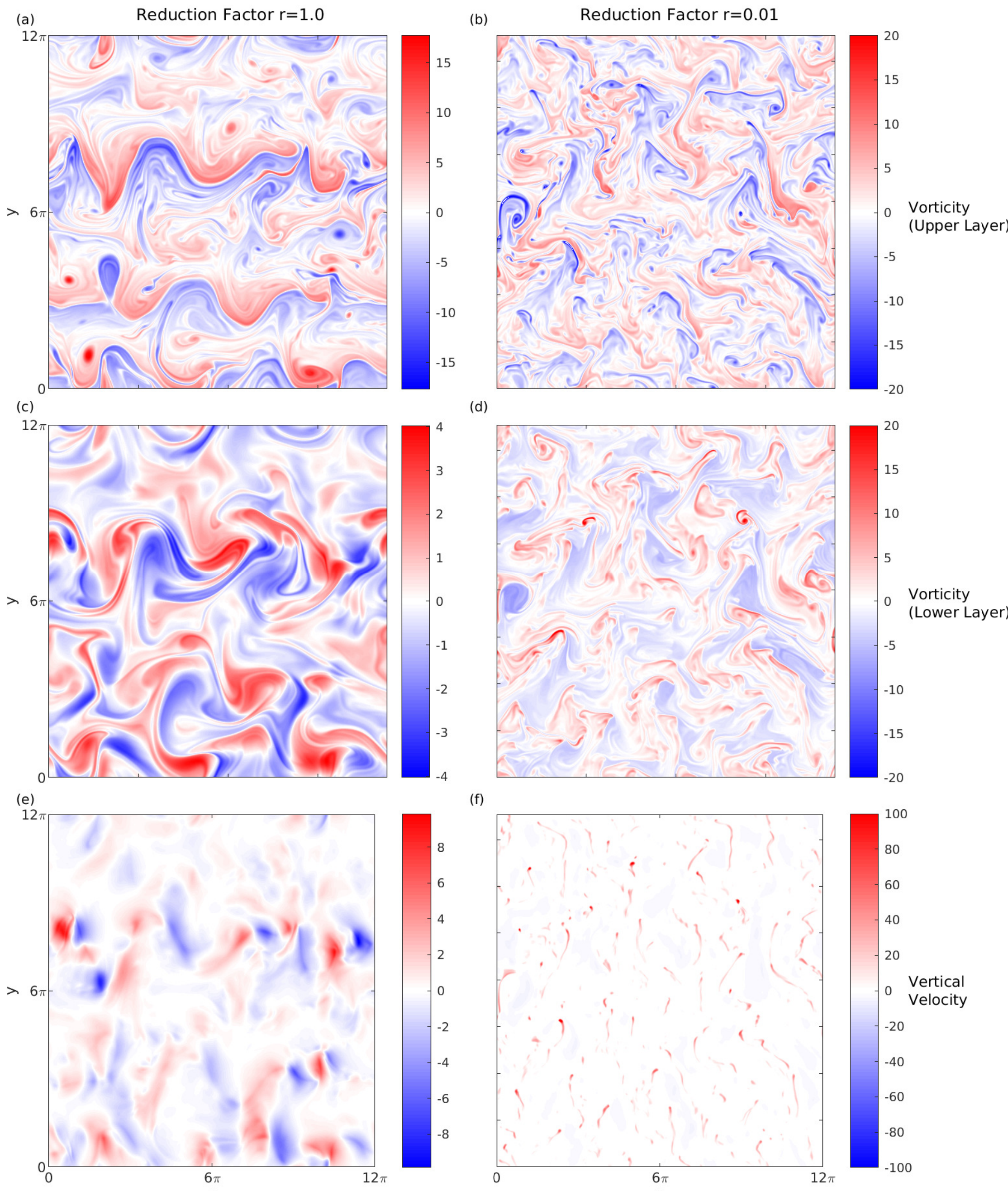

FIG. 1. Snapshots of relative vorticity in the upper layer (a,b) and lower layer (c,d), and vertical velocity (e,f) in the moist two-layer QG simulations at statistical equilibrium for $r = 1.0$ (a,c,e) and $r = 0.01$ (b,d,f). The flow transitions from a wavy jet state interspersed with vortices at $r = 1.0$ to a vortex dominated flow at $r = 0.01$. The vortices migrate poleward over time leaving a trail that can be seen in the vertical velocity snapshot in (f) and also more clearly over time in Supplementary Video S2. Note that different colorbar ranges are used for left and right panels.

drag, so that changes to β make little difference. Indeed, the unimportance of advection across the mean meridional PV gradient in the simulation is consistent with a vortex dominated rather than wavy flow. The vortices propagate northwards in our simulations through nonlinear advection and the trails of this propagation can be seen in the form of tendrilly north-south structures that are easiest to see in the vertical velocity field. This is particularly evident by looking at an animation of the evolution of the flow over time (Supplemental Video S2).

The vertical velocity field in the moist QG simulation has narrow regions of strongly ascending motion compared to wide regions of weakly descending motion (Fig. 1 f). We measure this asymmetry of the vertical velocity distribution using the vertical-velocity asymmetry parameter λ which appears in the effective static stability of O'Gorman (2011). For a vertical velocity with zero mean, $\lambda = 0.5$ corresponding to a symmetric distribution and $\lambda = 1$ corresponds to the limit in which updrafts are infinitely fast and narrow. The moist QG simulation at $r = 0.01$ has a remarkably high value of $\lambda = 0.94$. By contrast the asymmetry parameter is much lower at $\lambda = 0.73$ for idealized GCM simulations at the same $r = 0.01$ (O'Gorman et al. 2018). Kohl and O'Gorman (2024) introduced a simple toy model for λ in macroturbulent flow based on the moist QG omega equation which was able to roughly predict λ in the idealized GCM simulations and in reanalysis data. The key assumption of the toy model is that the dynamical forcing on the right-hand side of the moist omega equation is unskewed for macroturbulent flow, and this is found to also be the case in the QG simulations shown here. As shown in Appendix B, the toy model for λ correctly predicts that the QG simulations have a higher λ than the idealized GCM in part because the overall length scale of the flow becomes smaller when the vortex regime emerges. Thus DRV world illustrates that high λ is in principle possible in macroturbulent flow even if it is not seen so far in reanalysis or in GCM simulations.

A similar transition to a vortex dominated state in the strong latent heating regime has first been observed by Lapeyre and Held (2004) in a moist-two layer QG system using prognostic moisture. A comparison of our simulations to the results of Lapeyre and Held (2004) and Brown et al. (2023) is given in Appendix A, showing similarities in terms of energy spectra and the transition threshold for a vortex dominated flow, but also a difference in terms of the magnitude of skewness of the lower-layer vorticity in the vortex regime. In addition, Lapeyre and Held (2004) found that strong vortices had the same sign of vorticity in both layers (even if the upper layer vorticity was

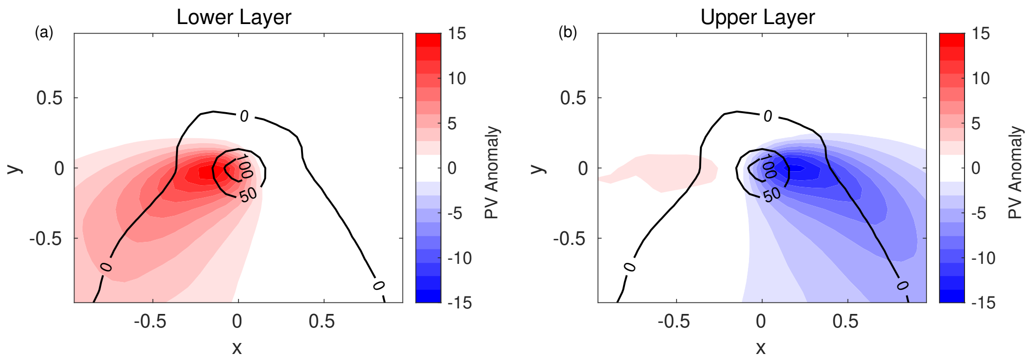

FIG. 2. Storm composite of the PV anomaly (shading) in (a) the lower layer, and (b) the upper layer of the moist QG turbulence simulations at $r = 0.01$. The vertical velocity is also shown (black contour); note negative velocities are too weak to be shown at the chosen contour interval of 50. Composites were created by averaging over the 10 strongest vertical velocity maxima at each simulation output between $t = 40-120$ when the simulation had reached a macroturbulent state.

weaker), whereas the vortices in our simulation have a baroclinic structure consisting of dipoles of positive PV anomalies in the lower layer and negative PV anomalies in the upper layer. Further work comparing simulations with the r parameterization of latent heating vs. prognostic moisture equations would be helpful to better understand these differences.

c. Storm Composites of PV and Dynamical Balances in DRV World

Fig. 2 shows the storm composite of the PV anomaly and vertical velocity in the upper and lower layer of the moist QG runs at $r = 0.01$. Composites were created by averaging over the 10 strongest vertical velocity maxima at each simulation output time between $t = 40-120$ when the simulation had reached a macroturbulent state. The PV takes on the typical dipole structure of DRV modes with a positive PV anomaly in the lower layer and a negative PV anomaly in the top layer (e.g., Kohl and O'Gorman 2022). The PV anomalies are displaced horizontally such that the updraft occurs east of the low level positive PV anomaly and west of the upper level negative PV anomaly. The updraft may be thought of as resulting from the poleward motion induced by the PV anomalies which leads to isentropic upgliding in the presence of a meridional temperature gradient. 'Trails' of PV can be seen to go southward because the storms are moving northward.

Further insights into the dynamical balances maintaining the storms can be obtained by studying the tendencies in the PV budget. In the lower layer, the PV budget is given by

$$\partial_t q_2 = q_{2x} - v_2 \bar{q}_{2y} - J(\psi_2, q_2) + (1 - r(w))w - R\nabla^2\psi_2 - \alpha\tau + \overline{r(w)w} - \mu\nabla^4 q_2, \tag{8}$$

where $q_2 = \nabla^2\psi_2 + (\psi_1 - \psi_2)/2$ is the PV anomaly in the lower layer, $\partial_t q_2$ is the time tendency of the PV in the lower layer, q_{2x} is PV advection by the mean zonal wind, $-v_2\bar{q}_{2y}$ is advection of the mean PV gradient by the meridional wind ($\bar{q}_{2y}$ includes contributions from both the mean temperature gradient and β), $-J(\psi_2, q_2)$ is the nonlinear advection, $(1 - r(w))w$ is the diabatic PV tendency from latent heating, $-R\nabla^2\psi_2$ is the drag term, $-\alpha\tau$ is the large-scale radiative damping, $\overline{r(w)w}$ is the spatially uniform radiative cooling, and $-\mu\nabla^4 q_2$ is the hyper-diffusion. The composite of the PV tendencies in the lower layer are shown in Fig. 3 centered on the vertical velocity maxima. As can be seen from Fig. 3a, the net effect of all tendencies is to give poleward propagation and amplification of the PV anomaly. The PV tendencies are dominated by mean zonal PV advection, nonlinear advection and diabatic generation from latent heating. Meanwhile, the drag term, diabatic generation from radiation (large scale radiative damping and spatially uniform radiative cooling), hyper-diffusion and the meridional advection of mean meridional PV gradients play a negligible role. This confirms the strong diabatic character of the storms in this regime with small r and thus strong latent heating.

Fig. 4 shows a cross-section through the PV tendencies of Fig. 3 averaged between $-0.2 < y < 0.2$. From left to right, we observe that in the descending part of the solution to the west ($-1 < x < -0.4$), where the diabatic generation from latent heating is zero, the PV tendency is given by the sum of mean zonal and nonlinear advection (with nonlinear advection the slightly more dominant contribution). In the ascending part of the solution ($-0.4 < x < 0.4$), the PV tendency is the result of a three way balance between diabatic generation from latent heating, zonal advection and nonlinear advection. Here mean zonal PV advection plays a more dominant role than nonlinear advection. In the descent region to the east of the ascent area ($0.4 < x < 1$), a negative PV tendency is caused by nonlinear advection with all other terms being negligible.

The dynamical balances governing the storms are very similar to that of the small-amplitude DRV mode of Kohl and O'Gorman (2022) with the addition of a nonlinear term that gives poleward advection, which leads us to the conclusion that the storms are indeed DRVs and that the statistical

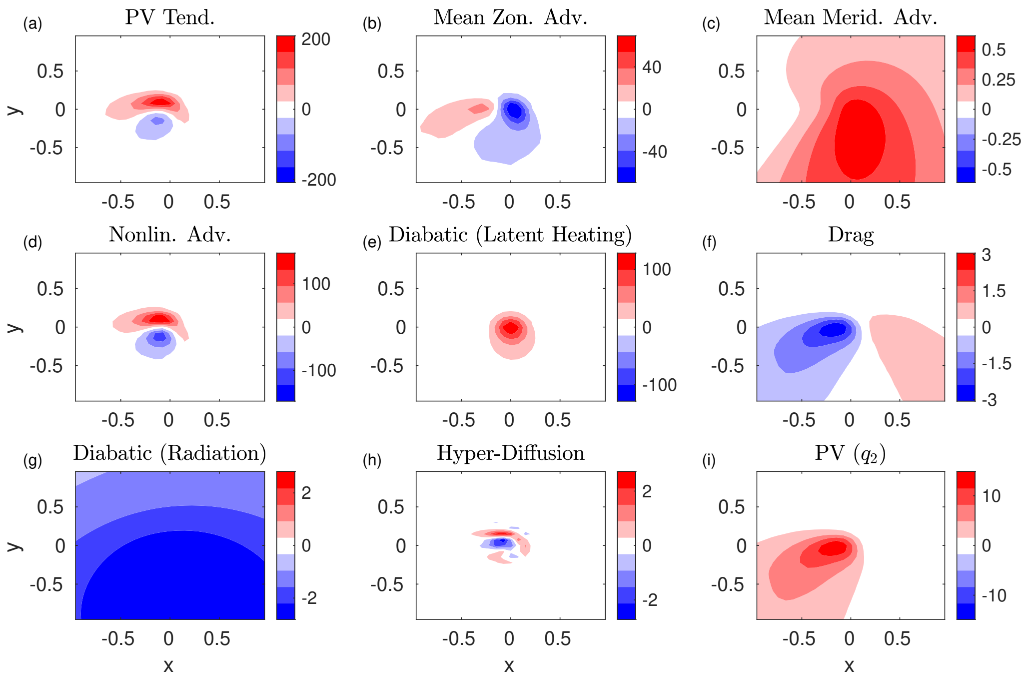

FIG. 3. Composite of the PV tendencies in the lower layer for the storms in the two-layer moist QG turbulent simulation at $r = 0.01$ showing (a) PV tendency q_{2t}, (b) mean zonal advection q_{2x}, (c) mean meridional advection $-v_2\bar{q}_{2y}$, (d) nonlinear advection $-J(\psi_2, q_2)$, (e) diabatic generation from latent heating$(1-r(w))w$, (f) drag $-R\nabla^2\psi_2$, (g) diabatic generation from radiation $-\alpha\tau + \overline{r(w)w}$ (large-scale radiative damping and spatially uniform radiative cooling), and (h) hyper-diffusion $-\mu\nabla^4 q_2$. Also shown to help interpretation is (h) the lower-layer PV (q_2). Composites were created by averaging over the 10 strongest vertical velocity maxima at each simulation output between $t = 40 - 120$ when the simulation had reached a macroturbulent state. The mean meridional advection and diabatic tendency from latent heating are proportional to lower-layer meridional velocity v_2 and the midlevel vertical velocity w, respectively. Note that the mean zonal wind in the lower layer is westward, and that different panels use different colorbar ranges.

equilibrium of the simulation is a DRV world. The main difference with the mode is the addition of nonlinear advection. Looking at the structure of the nonlinear advective tendency in Fig. 3d, we see that it is causing the poleward propagation that is evident in the net PV tendency and in Supplemental Video S2. Note that if we had used a basic state with westerly winds in the lower layer, the storms would also propagate eastwards. Poleward self advection is not found as strongly for the DRV storms observed in the current climate, which primarily have an eastward propagation (Boettcher and Wernli 2013). However, poleward propagation is found for a DRV storm identified

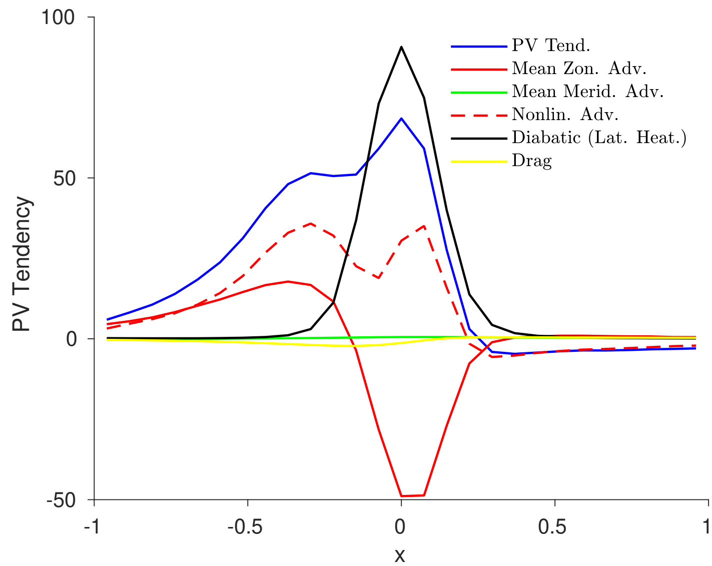

FIG. 4. Cross section through the PV tendencies in the lower layer shown in Fig. (3) averaged between $-0.2 < y < 0.2$. Colored lines show the PV tendency q_{2t} (blue), mean zonal advection q_{2x} (red), mean meridional advection $-v_2\bar{q}_{2y}$ (green), nonlinear advection $-J(\psi_2, q_2)$ (red dashed), diabatic generation from latent heating $(1-r(w))w$ (black), and the drag $-R\nabla^2\psi_2$ (yellow). Note that for the PV tendency and nonlinear advection, the meridional average includes both positive and negative contributions. We do not show the diabatic contribution from radiation and the hyper-diffusion since they were found to be small (see Fig. 3).

in the warm climate regime of idealized GCM simulations (see Fig. 1 of Kohl and O'Gorman 2022). Self-advection relies on the interaction between the lower positive PV anomaly and the upper negative PV anomaly, with the meridional winds induced by each PV anomaly advecting the other PV anomaly poleward.[3] We speculate that such poleward self-advection is weaker in DRVs in the current climate, because of reduced upper level negative PV anomalies as discussed in the next section.

Similar results for the vertical PV structure and the dynamical balances have been found by compositing on the lower-layer PV anomaly, rather than the vertical velocity, with the exception that the upper-layer negative PV anomaly is weakened compared to the lower-layer PV anomaly, and the PV tendency implies northwestward propagation instead of northward propagation (not shown).

[3] The self-advection by two opposite signed QG PV anomalies in different layers is like that of 'hetons' as discussed in Hogg and Stommel (1985), and it is distinct from the beta drift experienced by tropical cyclones.

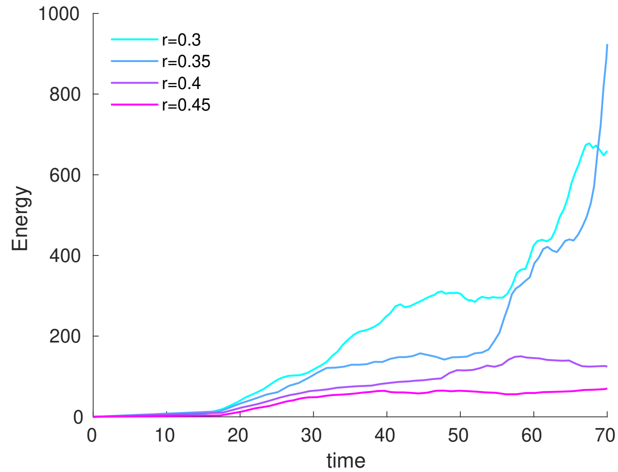

FIG. 5. Domain mean energy of the two-layer moist QG simulations versus time for different values of r. No linear radiative damping was applied in these simulations ($\alpha = 0$). Simulations below a value of $r < 0.4$ exhibit strong growth of a single vortex in the domain and a blow-up of energy over time.

d. Quantifying the Transition to DRV World

In this section, we seek to quantify the transition to DRV world as r is decreased and latent heating becomes stronger. One sign of a transition to vortices dominating the flow is that when the QG simulations are run without linear radiative damping ($\alpha = 0$), the simulations do not reach a statistical equilibrium for $r \lesssim 0.4$. Instead a single vortex in the domain grows rapidly to large size and become very energetic such that the domain-mean energy blows up rather than equilibrating (in practice the adaptive timestep in the solver becomes smaller and smaller, and we terminate the simulation). Fig. 5 shows the domain mean energy $\overline{(\nabla\phi)^2 + (\nabla\tau)^2 + \tau^2}$ as a function of time for a series of simulations at selected r values with $\alpha = 0$, illustrating the energy blow up for $r \lesssim 0.4$.

Interestingly, the energy blow-up threshold of $r \simeq 0.4$ is close to the exact threshold of $r = 0.38$ below which DRV modes can exist in an infinite domain in the tilted moist two-layer model (see Fig. 6 of Kohl and O'Gorman (2022)). Thus small-amplitude modal theory seems to provide an estimate for the r value at which DRV world starts to emerge, at least as measured by the need for radiative damping to equilibrate the vortices. But it is somewhat surprising that the infinite-domain result in the tilted model (which has no basic-state PV gradients) seems to be relevant to macroturbulence with PV gradients in a finite domain. When Kohl and O'Gorman (2022) analyzed the moist instability in a finite domain with basic-state PV gradients, there was no obvious threshold from wave to vortex modes at $r = 0.4$ (see Fig. 9a in Kohl and O'Gorman (2022)). However, it is possible that the finite amplitude vortices are different from the modes in this regard because meridional PV advection plays less of a role for the finite amplitude vortices considered here compared to small-amplitude modes. This could make the fully tilted model – without PV gradients – a better analogy for the fully turbulent simulations. The question of why the infinite-domain result is relevant remains open.

To further quantify the transition to DRV world, we have performed a second set of simulations using a constant radiative forcing rate $\alpha = 0.15$ spanning values of $r = 0.3 - 1$. The value $\alpha = 0.15$ was chosen as an intermediate value that doesn't overly damp the $r = 1$ simulation but still allows equilibration of the $r = 0.3$ simulation. The simulations are run until $t = 250$ and outputted every $\Delta t = 2$ times. The aim here is quantify the emergence of DRV world without the complicating factor of increases in the minimum required α for statistical equilibration as r is lowered. Snapshots of the resulting relative vorticity field in the upper layer are shown in Fig. 6 for a select number of r values. Note that for the value of α used here an equilibrated state would not be reached for r less than 0.3, and that the flow at $r = 1$ appears to be somewhat over damped. As r is lowered the flow field becomes increasingly populated by small-scale vortices (Fig. 6).

We quantify the transition to DRV world by introducing two metrics $\mathcal{M}_1$ and $\mathcal{M}_2$ that are inspired by our PV-based understanding of the growth of DRVs:

$$\mathcal{M}_1 = \frac{max((q_1\dot{q}_1 + q_2\dot{q}_2)^2)}{max(q_1^2 + q_2^2)\, max(q_{1t}^2 + q_{2t}^2)}, \tag{9}$$

$$\mathcal{M}_2 = \frac{max((q_1\dot{q}_1 + q_2\dot{q}_2)^2)}{max((q_1^2 + q_2^2)^2)}, \tag{10}$$

where q_i are the PV anomalies in each layer,$\dot{q}_i$ are the PV tendencies from latent heating in each layer, and q_{it} are the partial derivatives of the PV anomalies in each layer with respect to time. The maximum functions are taken as a spatial maximum for each snapshot, and the maximum could be at different locations for different maxima in the definition. The numerator of both metrics measures the collocation of PV anomalies with diabatic PV generation of the same sign which is a hallmark of latent-heating driven storms. $\mathcal{M}_1$ is normalized in such a way that it is dimensionless, and approaches 1 as the storms become diabatically dominated. We refer to it as the moist storm metric. $\mathcal{M}_2$ is normalized in such a way that it can be interpreted as a growth rate of moist storms,

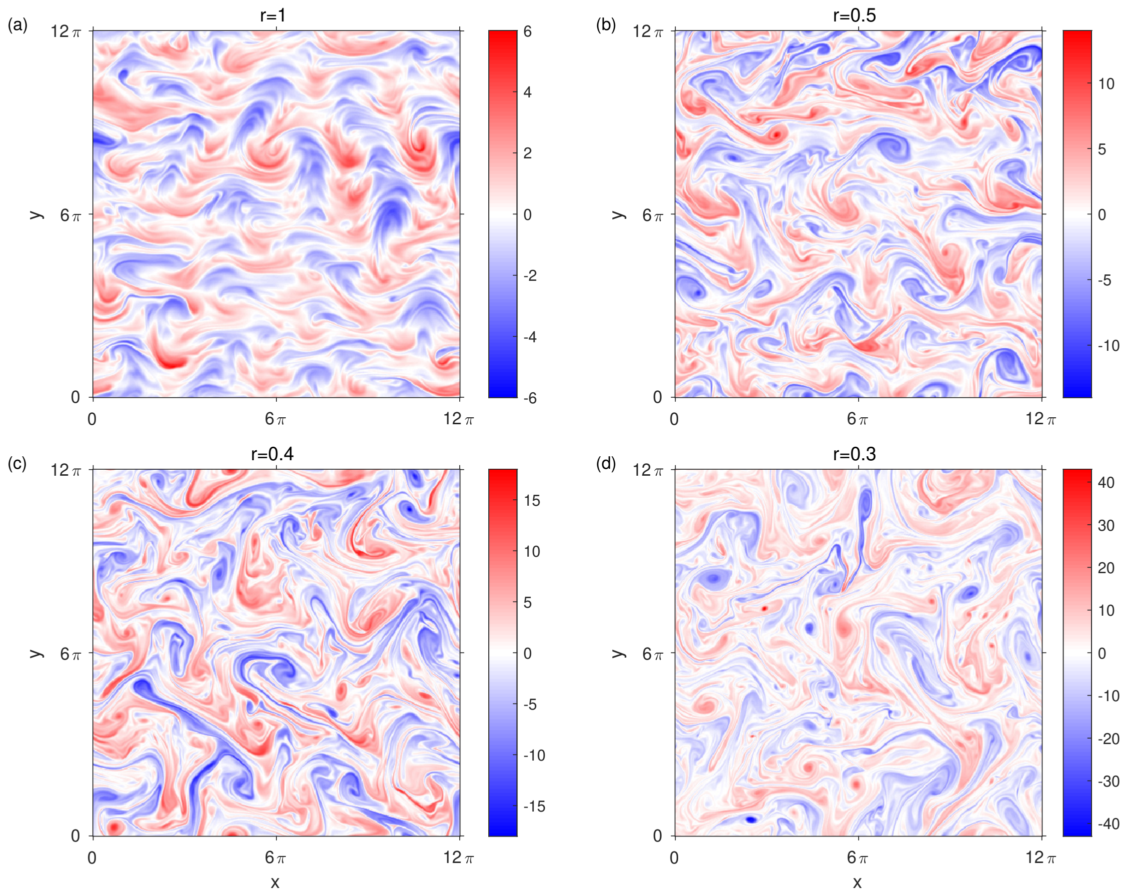

FIG. 6. Snapshots of the relative vorticity in the upper layer of the moist QG simulations for (a) $r = 1$, (b) $r = 0.5$, (c) $r = 0.4$, and (d) $r = 0.3$. All simulations shown were run with the same radiative damping rate of $\alpha = 0.15$. As r is lowered, the flow becomes increasingly dominated by small-scale vortices. Note that different panels use different colorbar ranges.

and we refer to it as the moist growth rate metric. For each simulation, the metrics were calculated between $t = 100-250$ in the turbulent phase of the simulation and then averaged in time. The results are shown in Fig. 7a,b as a function of r. Both metrics increase exponentially as r is reduced with a marked increase for $r < 0.5$. For $\mathcal{M}_2$, the increase is much more rapid than implied by "Clausius-Clapeyron scaling" (i.e., the increase in latent heating from reducing r at fixed w which would would imply $\mathcal{M}_2 \sim (1-r)^2$). Taken together, the behavior of the moist storm and moist growth rate metrics versus r and the equilibration behavior of the simulations without radiative damping suggest that DRV world begins to emerge at approximately $r = 0.4$.

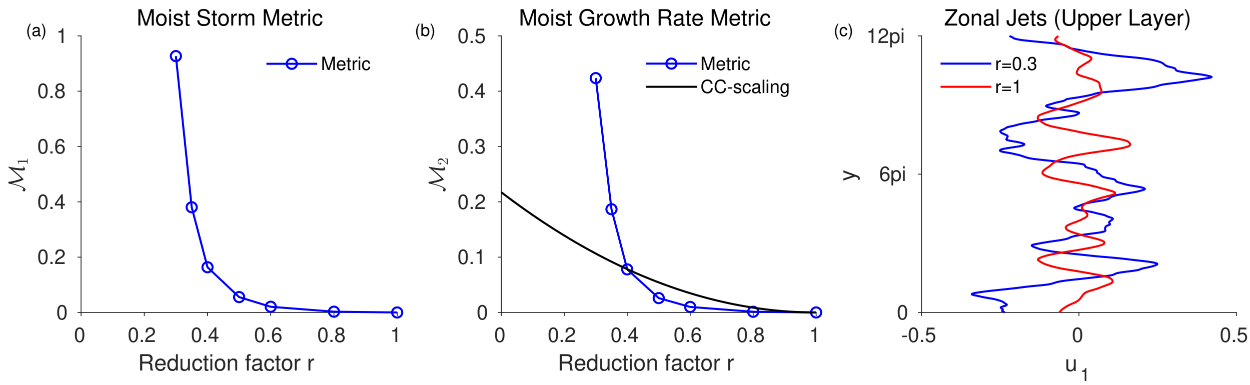

FIG. 7. Quantifying the transition to DRV world in QG simulations with fixed radiative damping of $\alpha = 0.15$: (a) the time-mean moist storm metric $\mathcal{M}_1$ as a function of r, (b) the time-mean moist growth rate metric $\mathcal{M}_2$ as a function of r, and (c) zonal- and time-mean zonal wind in the upper layer for $r = 0.3$ (blue) and $r = 1.0$ (red). For (b), the black line shows Clausius-Clapeyron scaling. For all panels, time averaging was over $t = 100 - 250$.

Remarkably, our transition threshold to DRV world of $r = 0.4$ is the same as the transition threshold to a vortex regime previously reported by Lapeyre and Held (2004) using a different moist QG model with a prognostic moisture equation. In particular, their reported threshold of $\mu_{\text{sat}} = 2.5$ corresponds to our threshold of $r = 0.4$ as shown in Appendix A. This correspondence suggests that the transition is not specific to the details of the latent heating parameterization.

The transition to a vortex dominated regime is also associated with changes in the jet structure. Fig. 7c shows the zonal- and time-mean zonal wind averaged over $t = 100 - 250$.[4] As r is lowered from $r = 1$ to $r = 0.3$, we find that the jet spacing widens. At $r = 0.3$, there are still jets present even though the flow field is dominated by vortices. At $r = 0.01$, the jets have completely vanished (Fig. 1). However, the simulation at $r = 0.01$ has to be run with a much stronger radiative damping ($\alpha = 1.7$ instead of $\alpha = 0.15$) to reach statistical equilibrium. Thus while it seems likely that the full disappearance of the jets at $r = 0.01$ is due to an even stronger vortex regime, we cannot rule out that it is caused by stronger radiative damping.

3. DRVs in Turbulent Simulations of the Moist Primitive Equation

We now investigate strong diabatic storms in a set of more realistic simulations using the moist primitive equations. After nondimensionalization, the governing parameter that will be investigated

[4]Experimenting with different averaging times, we note that while the jet positions are fairly stable at $r = 1$, they are less so at $r = 0.3$ and the jet position moves meridionaly over time.

is the Rossby number. Switching between high and low Rossby number regimes, while maintaining strong latent heating, will allow us to investigate the role of higher order terms in the PV dynamics beyond QG.

a. Model Formulation

The moist primitive equations in Boussinesq form, with constant planetary vorticity, r parametrization for latent heating, and Newtonian relaxation of temperature take the form

$$\frac{D\mathbf{u}}{Dt} + \mu_u \nabla^4 \mathbf{u} + f_0 \mathbf{k} \times \mathbf{u} = -\nabla\phi - R\mathbf{u}, \tag{11}$$

$$\frac{D\theta}{Dt} + \mu_\theta \nabla^4 \theta = (1-r) w \theta_z - \alpha(\theta - \theta_r), \tag{12}$$

$$u_x + v_y + w_z = 0, \tag{13}$$

$$\frac{g}{\theta_0}\theta = \phi_z, \tag{14}$$

$$\frac{D}{Dt} = \partial_t + u\partial_x + v\partial_y + w\partial_z, \tag{15}$$

$$\theta_r = \frac{z\theta_0 N^2}{g} - \frac{\theta_0}{g}\frac{f_0 U}{H} y, \tag{16}$$

where $\mathbf{u} = (u, v)$ is the horizontal velocity field, w is the vertical velocity field, ∇ is the horizontal gradient, ϕ is the geopotential height, θ is the potential temperature, θ_0 is the reference potential temperature, $\theta_r(y, z)$ is a zonally uniform reference state that is constant in time, f_0 is the constant Coriolis parameter, $r(w)$ is the nonlinear reduction factor, α is a radiative relaxation constant, g is the gravitational constant, H is the tropospheric height, U/H is the shear implied by thermal wind for the reference θ_r profile, N is a constant static stability, L_y is the domain length in the meridional direction, R is a drag coefficient, and (μ_u, μ_θ) are coefficients for horizontal hyperdiffusion.

The equations are being forced by relaxing θ at a rate α to a reference state θ_r with a constant static stability and a linear temperature variation in the meridional direction. In the vertical, the domain is bounded by vertical plates at $z = 0, H$ with boundary condition $w = 0$, where H now represents the full tropospheric depth. Linear drag and small-scale dissipation are applied in the momentum equations. We have found it helpful to use a drag that is constant throughout the troposphere (rather than confined to the lower levels) to prevent the build up of small-scale vertical velocities in the upper levels particularly at high Rossby number. This build up may be due to spurious wave reflections at the boundary, and for simplicity we use a vertically constant drag for all simulations.

The β term is neglected here, since it was found to be negligible in the QG simulations and it would introduce a term linear in y in the momentum equations that cannot be represented by the doubly-periodic Dedalus solver (Burns et al. 2020).

We make the model variables statistically homogeneous in the horizontal by considering the deviation θ' from the reference temperature, such that

$$\theta = \theta_r(y,z) + \theta'(x,y,z,t). \tag{17}$$

Similarly for geopotential, we define

$$\phi = \phi_r(y,z) + \phi'(x,y,z,t), \tag{18}$$

where

$$\phi_r = z^2 N^2/2 - f_0(U/H)yz. \tag{19}$$

Plugging these decompositions into Eqs.11-15 leaves us with

$$\frac{D\mathbf{u}}{Dt} + \mu_u \nabla^4 \mathbf{u} + f_0 \mathbf{k} \times \mathbf{u} = -\nabla\phi_r - \nabla\phi' - R\,\mathbf{u}, \tag{20}$$

$$\frac{D\theta'}{Dt} + v\theta_{r,y} + w\theta_{r,z} + \mu_\theta \nabla^4 \theta' = (1-r)w\theta_{r,z} + (1-r)w\theta'_z - \alpha\theta', \tag{21}$$

$$u_x + v_y + w_z = 0, \tag{22}$$

$$\frac{g}{\theta_0}\theta' = \phi'_z, \tag{23}$$

$$\frac{D}{Dt} = \partial_t + u\partial_x + v\partial_y + w\partial_z, \tag{24}$$

We note that $\mathbf{u}$ includes the mean vertical shear unlike in the two-layer QG model where we defined a perturbation baroclinic streamfunction.

Next, we nondimensionalize the equations using QG scaling (but keeping all terms) such that $x, y \sim L_D$ with deformation radius[5] $L_D = NH/f_0$, $z \sim H$, $t \sim L_D/U$, $\mathbf{u}, \mathbf{v} \sim U$, $w \sim \epsilon UH/L_D$ where $\epsilon = U/f_0 L_D$ is the Rossby number, $\phi' \sim f_0 U L_D$, $\theta' \sim \theta_0 f_0 U L_D / gH$ to obtain the nondimensionalized equations

$$\epsilon \frac{D\mathbf{u}}{Dt} + \widetilde{\mu_u}\nabla^4\mathbf{u} + \mathbf{k}\times\mathbf{u} = z\mathbf{e_y} - \nabla\phi' - \widetilde{R}\mathbf{u}, \tag{25}$$

$$\frac{D\theta'}{Dt} - v + w + \widetilde{\mu_\theta}\nabla^4\theta' = (1-r)w + \epsilon(1-r)w\theta'_z - \widetilde{\alpha}\theta', \tag{26}$$

$$u_x + v_y + \epsilon w_z = 0, \tag{27}$$

$$\theta' = \phi'_z, \tag{28}$$

$$\frac{D}{Dt} = \partial_t + u\partial_x + v\partial_y + \epsilon w\partial_z, \tag{29}$$

with nondimensional numbers $\epsilon = \frac{U}{f_0 L_D} = \frac{U}{NH}$, $\widetilde{R} = \frac{1}{f_0}R$, $\widetilde{\alpha} = \frac{L_D}{U}\alpha$, $\widetilde{L_y} = \frac{1}{L_D}L_y$, $\widetilde{\mu_u} = \frac{1}{f_0 L_D^4}\mu_u$, and $\widetilde{\mu_\theta} = \frac{1}{UL_D^3}\mu_\theta$ and unit vector in the meridional direction $\mathbf{e_y}$.

We note that as a result of scaling horizontal length scales with the deformation radius, what we refer to as the Rossby number in these simulations $\epsilon = \frac{U}{f_0 L_D}$ could also be interpreted as the Froude number $\frac{U}{NH}$ or the inverse square root of the Richardson number $\frac{N^2H^2}{U^2}$. We stick to the designation of Rossby number here to reflect the intuition that a low Rossby number limit recovers QG dynamics. Furthermore, we note that in the definition of the Rossby number U/H should be interpreted as the mean-state zonal wind shear (rather than, say, the local wind shear in a storm) and as such $\epsilon = U/NH$ refers to a mean-state Rossby number rather than the Rossby number of an individual storm (which could be much higher).

The equations are solved using a spectral solver with adaptive time stepping (Burns et al. 2020) on a doubly periodic square domain of side $\widetilde{L_y} = 6\pi$, with horizontal plates at $z = 0$ and $z = 1$ and $128\times128\times10$ grid points. Chebyshev polynomials are used as basis functions in the vertical (the grid spacing between the 10 vertical levels is close to uniform in the interior but slightly smaller towards the boundaries). The simulations are initialized with random conditions for all fields, after

[5]The definition of the deformation radius is different here from the QG system discussed in section 2 because H now refers to the full tropospheric height, and we have dropped the $\sqrt{2}$. We will see from the numerical simulations that scaling the length scale like the deformation radius remains a reasonable choice for the PV anomalies even in the presence of strong latent heating. In the DRV modal theory of Kohl and O'Gorman (2022), the ascent length scale vanishes as $r \to 0$, but the PV anomaly in the descent area is sustained by a balance of growth and zonal advection leading to an exponential decay length L_D/σ where σ is the growth rate. But since the growth rate approaches $\sigma = 1.62$ in the limit of $r \to 0$, the length scale of the PV disturbance also remains finite in this limit, at roughly $0.62L_D$ which is close to L_D.

filtering out all wavenumbers with $k = \sqrt{k_x^2 + k_y^2} > 3$ to avoid having to integrate a lot of small scale noise in the initial phase of the simulation. The simulations are run until $t = 160$ and outputted every $\Delta t = 0.5$.

We run simulations with a high Rossby number $\epsilon = 0.4$, an intermediate Rossby number $\epsilon = 0.1$, and a low Rossby number $\epsilon = 0.01$ while keeping the latent heating strong at $r = 0.01$ in all cases. For reference, using typical scales $U = 10\text{m s}^{-1}$, $L_D = 1000\text{km}$ and $f_0 = 10^{-4}\text{s}^{-1}$, suggesting that the intermediate Rossby number $\epsilon = U/f_0L_D = 0.1$ is closest to typical Earth-like conditions. Thus, low and high Rossby number refer to Rossby numbers that are low and high relative to this Earth-like value.

The drag coefficient and momentum hyperdiffusion coefficient need to be smaller in the intermediate and low Rossby regime to avoid over-damping the simulations. Given that the time derivative of horizontal momentum is multiplied by ϵ in Eq. 25, we held $\widetilde{R}/\epsilon$ and $\widetilde{\mu}_u/\epsilon$ approximately constant as the Rossby number changes, which in the limit of vanishing Rossby number is consistent with QG scaling. For the high Rossby number run, we choose $\widetilde{R} = 0.11$ and $\widetilde{\mu}_u = 5 \times 10^{-5}$, for the intermediate Rossby number run $\widetilde{R} = 2.75 \times 10^{-2}$ and $\widetilde{\mu}_u = 1.25 \times 10^{-5}$, and the low Rossby number run $\widetilde{R} = 2.75 \times 10^{-3}$ and $\widetilde{\mu}_u = 1.25 \times 10^{-6}$. The hyperdiffusion for temperature is $\mu_\theta = 5 \times 10^{-5}$ in all cases.

The radiative relaxation coefficient was chosen to be $\alpha = 0.35$ for the high Rossby number simulation and $\alpha = 0.6$ for the intermediate and low Rossby number simulations. A higher relaxation coefficient was found to be necessary at intermediate and low Rossby numbers in order to stabilize the simulations. As we will see in the next section, while the simulations at intermediate and low Rossby number transition to DRV world similar to the QG simulations, the simulation at high Rossby number does not transition to a DRV world. The need for a stronger relaxation with onset of the vortex regime is hence consistent with what was found for the QG simulations in which radiative damping was needed for equilibration when a DRV world emerged. We also explored primitive-equation simulations in which the background temperature gradient was not imposed but rather the temperature was relaxed to a cosinusoidal reference temperature. Thus, the radiative forcing is not as strong, and it is easier for the flow to equilibrate. Note that the cosinusoidal reference temperature was chosen because relaxation to a linear gradient is not possible in a doubly periodic solver. In this case we found that it is possible to run the simulations with the same relaxation coefficient for all Rossby numbers. Transition to DRV world at low Rossby number persists and the structure of storms is similar to what we present in the next section. We stick to the linear temperature gradient set-up here because its interpretation is simpler, and it makes a closer connection to the QG simulations discussed previously in section 2.

b. Simulation Results

Fig. 8 shows snapshots of the relative vorticity at a lower level ($z = 0.15$) and an upper level ($z = 0.85$), and the vertical velocity around mid-level ($z = 0.42$) in the macroturbulent phase of the simulations for the low and high Rossby number simulations.

In the low Rossby number simulation (Fig. 8a,c,e), the character of the flow is dramatically different from that in Earth's midlatitude atmosphere. The flow field is not wave-like and is disrupted by vorticity dipoles, positive in the lower layer and negative in the upper layer of roughly equal strength. The vorticity dipoles continuously spawn and rapidly propagate poleward as can be most clearly seen in Supplemental Video S3. Similarly, the vertical velocity field breaks up into isolated vertical velocity maxima, associated with the vorticity dipoles, and is characterized by a large vertical-velocity asymmetry parameter $\lambda = 0.88$. The simulation is clearly a DRV world similar to the strong latent heating regime of the moist QG simulations.

In the high Rossby number simulation (Fig. 8 b,d,f), by contrast, the vorticity in the upper troposphere is more wave-like and larger in scale. In the lower-troposphere, there are still smaller-scale vortices but these are now associated with prominent frontal bands. The vorticity field is stronger in the lower troposphere compared to the upper troposphere. The storms evolve more slowly, and while they still drift poleward, their primary propagation is eastward, as can be seen in Supplemental Video S4. The vertical velocity field is made up of frontal bands and localized maxima, resembling the midlatitude vertical velocity field in Earth's atmosphere. The vertical velocity asymmetry parameter is $\lambda = 0.75$ which is similar to what was found in the reduced stability GCM simulations of O'Gorman et al. (2018) at $r = 0.01$. The flow does not show signs of transition to a purely vortex dominated regime despite the strong latent heating.

In the intermediate Rossby number simulation (Supplemental Video 5), the flow is vortex dominated, and we consider it to be still a DRV world. A stream of vortices that continously spawn and quickly propagate poleward can be clearly seen. However, the flow also retains some

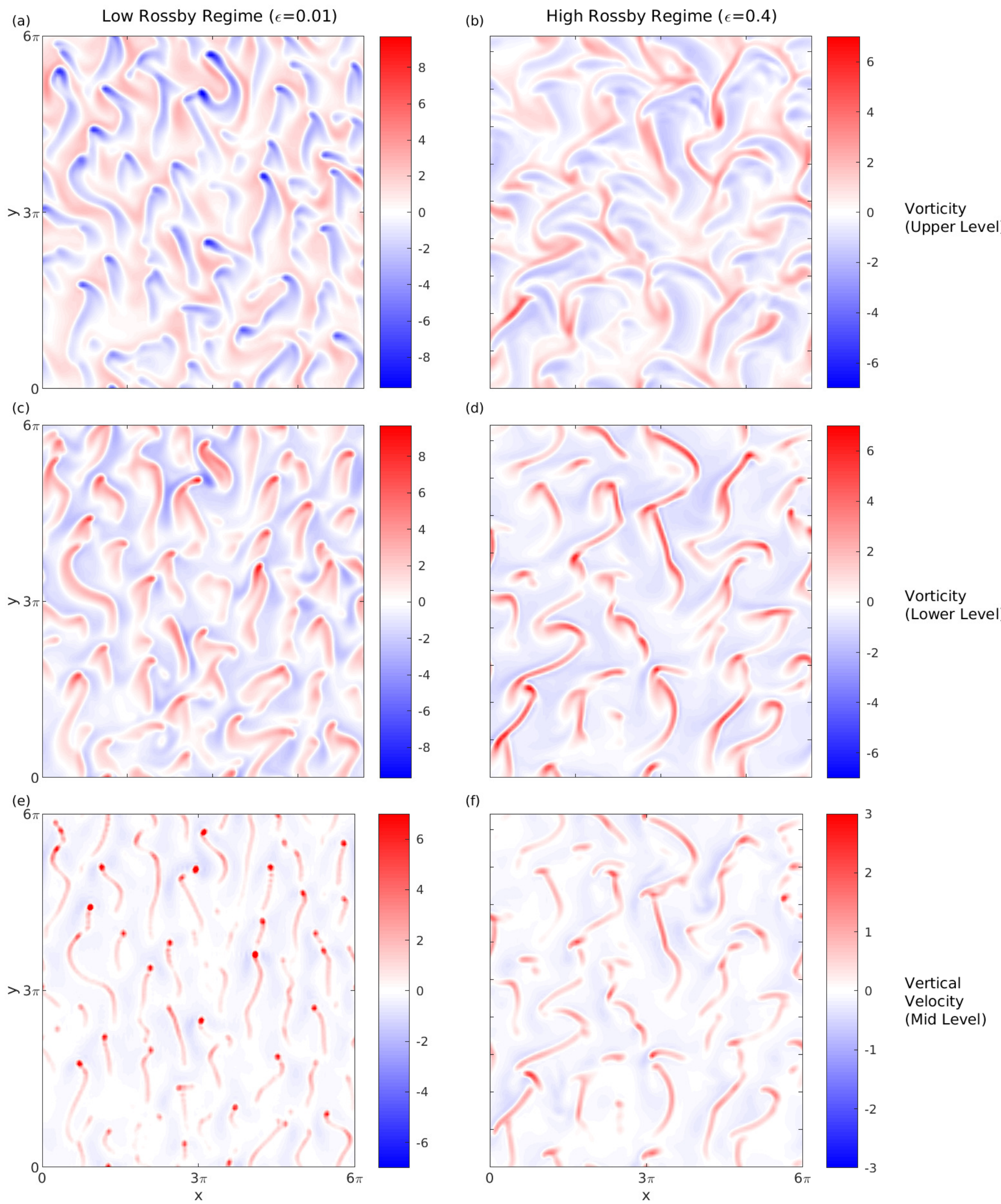

FIG. 8. Snapshots of the relative vorticity at a lower ($z = 0.15$) and upper level ($z = 0.85$) and vertical velocity ($z = 0.42$) around mid-level for (a,c,e) a low Rossby number simulation ($\epsilon = 0.01$), and (b,d,f) a high Rossby number simulation ($\epsilon = 0.4$) run in the moist primitive equation simulations at $r = 0.01$. At low Rossby number, the flow is a DRV world with vorticity dipoles that propagate poleward. At high Rossby number, the poleward propagation is slower and the flow has both vortices and fronts. Animations of the two simulations can be found in Supplemental Videos S3 and S4. Note that different panels use different colorbar ranges.

frontal features that were observed in the high Rossby number simulation. We conclude that the transition to a DRV world with decreasing Rossby number is gradual rather than abrupt.

Next we turn to the PV structure of the storms for the high and low Rossby number simulations. We calculate the Ertel PV

$$Q = (1+\epsilon\zeta)\theta_z - \epsilon^2 v_z\theta_x + \epsilon^2 u_z\theta_y, \tag{30}$$

where $\zeta = v_x - u_y$ and $\theta_z = 1+\epsilon\theta_z'$, and subtract the zonal mean to define the PV anomalies. We also calculate the PV tendency from latent heating

$$\dot{Q}_{\mathrm{LH}} = \epsilon(1+\epsilon\zeta)\dot{\theta}_z, \tag{31}$$

where $\dot{\theta} = [(1-r(w))w\theta_z]$, and we have ignored contributions due to horizontal gradients of the heating profile. Equations 30 and 31 are derived in Appendix C. We then composite PV anomalies and PV tendencies over the 10 strongest vertical velocity maxima at each simulation output between $t = 70-160$ when the simulations are in statistical equilibrium. The results are shown in Figure 9 a,b,c for the low, intermediate and high Rossby number simulations.

While the low Rossby number storms show a clear dipole structure both in terms of PV anomaly and PV tendency (Fig. 9a), the high Rossby number storms are made up of a strong low level positive PV anomaly only (Fig. 9c). No strong negative PV anomaly is visible at the location of negative diabatic PV generation, although a weaker positive and negative PV anomaly signal is visible at the top boundary. Negative diabatic generation is weaker compared to positive diabatic generation. For the intermediate Rossby number regime, a clear negative PV anomaly is visible at the location of negative diabatic generation (Fig. 9b). Unlike in the low Rossby number case, at intermediate Rossby numbers the negative PV anomaly aloft is weaker compared to the low level positive anomaly. While diabatic generation extends over the entire vertical extent of the domain at low and intermediate Rossby number, diabatic generation remains mostly confined to the lower part of the domain at high Rossby number. Overall, Fig. 9a-c shows the weakening of upper level PV anomaly and diabatic generation as the Rossby number is increased.

If vertical PV advection $-\epsilon w Q_z$ is added to the PV tendency from latent heating (cf. Appendix C for derivation), the negative PV generation in the high Rossby number composite at $z = 0.5$ is

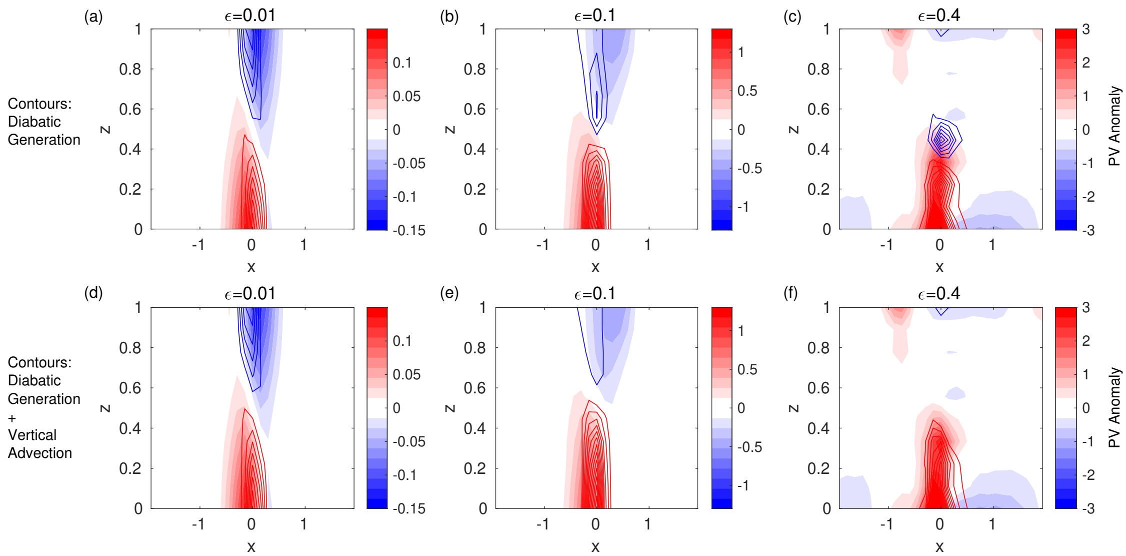

FIG. 9. Storm composite of Ertel PV anomaly (shading) and PV tendency from latent heating (contours) for (a) the low Rossby number simulation ($\epsilon = 0.01$),(b) the intermediate Rossby number simulation ($\epsilon = 0.1$) and (c) the high Rossby number simulation ($\epsilon = 0.4$). The contour interval is (a,d) 0.1, (b,e) 0.5 and (c,f) 2.1. The zero contour line for the PV tendencies is not shown. Panels (d,e,f) show the same storm composites for the low, intermediate, and high Rossby number simulation as in (a,b,c) but now the PV tendency includes the contributions from latent heating plus vertical advection. Composite means were made over the 10 strongest vertical velocity maxima at each output time between $t = 70-160$. Note the different color bar ranges for different Rossby numbers.

almost entirely canceled, with a weaker signal persisting at the upper boundary (Fig. 9f). By contrast, negative generation persists for the low and intermediate Rossby number storms (Fig. 9d,e).

The PV structure of the low Rossby number storm resembles that of the small-amplitude DRV mode from theory (Fig. 3 in Kohl and O'Gorman 2022), while the PV structure of the high Rossby number storm resemble that of DRVs from reanalysis in the current climate (Fig. 10 in Kohl and O'Gorman 2022). The Rossby number is low for small-amplitude modes and high for storms in reanalysis, and hence the similarity between the low Rossby numbers storms and DRV modes, and between the high Rossby number storms and DRV storms in reanalysis is as expected.

c. Discussion

The primitive-equation simulations with strong latent heating show that changes in the Rossby number bring about important changes both in terms of the PV structure of individual storms and in terms of the overall circulation. In particular, low Rossby numbers make the simulations more like DRV world in which diabatically maintained PV dipoles continuously spawn and propagate poleward. At higher Rossby number, DRVs still occur but they have a different PV structure, they do not propagate as quickly poleward and they do not fully dominate the flow which now also includes frontal features.

We note that for the high Rossby number storms (Fig. 9c), a weak positive PV anomaly at upper levels is visible westward of the strong low level positive PV anomaly, unlike in the low and intermediate Rossby number storms. This upper-level positive PV anomaly suggests that at high Rossby number there may be some growth induced from a type-C cyclogenesis mechanism as found in Ahmadi-Givi et al. (2004). We leave exploration of this to future work.

4. Toy Model for the Vertical Structure of PV in Finite Amplitude DRVs

We study a 1-D toy model for the vertical structure of PV in the ascent region of a DRV in order to understand why the PV structure is different at high versus low Rossby number. This model will also help to bridge the gap between the theory of DRV modes and finite-amplitude storms, although we emphasize that it is not a full model because the vertical velocity profile w will be taken as given. This approach is similar to previous studies of the PV evolution given prescribed vertical velocity or heating profiles (Schubert and Alworth 1987; Abbott and O'Gorman 2024). The model equations are the thermodynamic equation with reduced stability parameterization of latent heating and the PV evolution equation:

$$\partial_t \theta' + w\bar{\theta}_z + \epsilon w \theta'_z = \dot{\theta}, \tag{32}$$

$$\partial_t Q = \epsilon \frac{Q\dot{\theta}_z}{\bar{\theta}_z + \epsilon \theta_z} - \epsilon w Q_z, \tag{33}$$

where $\bar{\theta}_z$ represents a background stratification that is assumed constant in time, and $\dot{\theta} = (1 - r)w\bar{\theta}_z + \epsilon(1-r)w\theta'_z$ is the latent heating rate. We focus on a single vertical column ($0 \le z \le 1$) in a region of maximum heating in the horizontal such that $\dot{\theta}_x = \dot{\theta}_y = 0$, approximate the PV as

$Q = (1+\epsilon\zeta)\theta_z$, which ignores the terms $\epsilon^2 v_z\theta_x$ and $\epsilon^2 u_z\theta_y$, and ignore any horizontal PV transport. A derivation is given in Appendix D. The toy model is evolved forward in time for a high ($\epsilon = 0.4$), intermediate ($\epsilon = 0.1$) and low Rossby number ($\epsilon = 0.01$) with the aim of matching the storms found in the moist primitive equation simulations (Fig. 9). The integration is started from the initial conditions $\theta' = 0$ and $Q = \bar{\theta}_z$. For the low and intermediate Rossby numbers, we choose a constant background stratification $\bar{\theta}_z = 1$ to match what was found in the primitive-equation simulations at those Rossby numbers. For the high Rossby number regime, we also consider a bottom-heavy stratification $\bar{\theta}_z = 1 + 0.25e^{(-(z-0.2)/0.1)}$ in addition to the constant stratification case, since a bottom-heavy stratification is what was found for the storms in the high Rossby number regime (not shown). The bottom-heavy stratification results from vertical eddy heat fluxes which are larger at high Rossby number, and it leads to bottom-amplified heating rates, per the r parameterization of latent heating. The vertical velocity profile is fixed in time as $w = \sin(\pi z)$ which is symmetric about $z = 0.5$. A vertically constant profile is again chosen for r with a value of $r = 0.01$, but we note that vertical variations in r can matter in the atmosphere particularly in colder climates.

The equations are evolved forward in time until $t = 1.2$, which corresponds roughly to $t = 1.2L_D/U = 33$h using typical scales $L_D = 1000$km and $U = 10$m s^{-1}. The resulting PV anomaly profiles are shown in Fig. 10 where we have defined PV anomalies with respect to the initial PV profile.

We focus first on the low Rossby number case (Fig. 10a). The PV profile has the typical dipole structure seen in the moist QG storms (Fig. 2), low-Rossby number storms of the moist primitive equation simulations (Fig. 9a), and the DRV modes from theory (Kohl and O'Gorman 2022). The PV is antisymmetric about the altitude of maximum ascent $z = 0.5$. By contrast, the intermediate Rossby number case which also has a constant background stratification has stronger positive than negative PV anomalies (Fig. 10b) and its structure bears close resemblance to the storms found in the moist primitive equation simulations at intermediate Rossby number (Fig. 9b). The different magnitude of positive and negative PV anomalies arises because of the appearance of the PV in the diabatic generation term – the first term on the right-hand side of Eq. (33) – which amplifies the generation of positive PV anomalies but weakens the generation of negative PV anomalies, leading to a nonlinear feedback as the PV anomalies evolve. For the low Rossby number case (Fig.

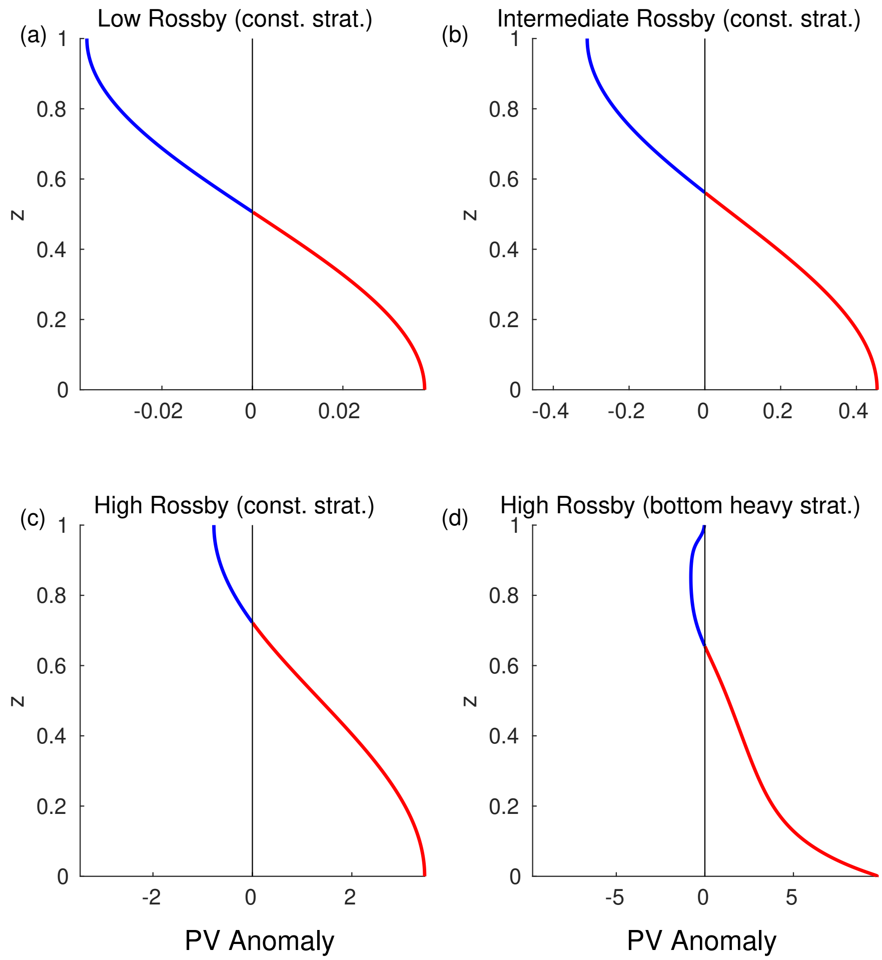

603 FIG. 10. PV anomaly profiles produced by the toy-model Eqs. (32-33) at $t = 0.5$ using a value of $r = 0.01$ for (a) a low Rossby number storm of $\epsilon = 0.01$, (b) an intermediate Rossby number storm of $\epsilon = 0.1$, and (c,d) a high Rossby number storm of $\epsilon = 0.4$. For panels (a-c) we use a constant background stratification, and for panel (d) we use a bottom-heavy stratification. The PV anomalies are defined with respect to the initial conditions. Negative anomalies are shown in blue and positive anomalies in red.

10a), this feedback is negligible because the PV anomalies are too weak to strongly affect the PV and thus too weak to affect the diabatic PV production, but for the intermediate Rossby number case (Fig. 10b) the feedback is important because the PV anomalies are larger. We also note that for the intermediate Rossby number case, vertical advection – the second term on the right-hand side of Eq. (33) – has begun to move the positive PV anomaly upwards so that the change from positive to negative PV anomaly no longer occurs at about $z = 0.5$ but instead at $z = 0.56$. If the time integration is continued, the positive PV anomaly would keep being advected vertically and gradually begin to fill up the entire vertical column until no negative PV anomaly is left (not shown). This limit is spurious however, since the assumption of a sustained vertical velocity profile would break down.

Looking at the high Rossby number case with constant stratification (Fig. 10c), we notice that the positive PV anomaly has grown even larger than for the intermediate Rossby number case. The PV structure is highly asymmetric in magnitude between positive and negative PV anomalies with the surface PV anomaly about 4.5 times stronger than the negative PV anomaly aloft. This is because the positive PV generation is larger at high Rossby number. When the calculation is repeated using a bottom heavy stratification (Fig. 10d), as was found for the high Rossby number storms in the simulation, the asymmetry between positive and negative PV values is even more pronounced, with surface anomalies 12 times stronger than PV anomalies aloft. This is because the bottom heavy stratification implies a bottom heavy heating rate. The vertical gradient of the heating rate, which affect the diabatic PV generation, is larger below the heating maximum, leading to stronger positive generation, and weaker above the heating maximum, leading to weaker negative PV generation. This signal then gets amplified by the nonlinear feedback between PV and the heating gradient leading to highly asymmetric bottom heavy storms as were found in the high Rossby number moist primitive equation simulations (Fig. 9c).

Due to the nonlinearity of the feedback between PV anomalies and diabatic PV generation, the strength of the low-level PV anomaly that is reached at the end of the integration is very sensitive to the magnitude of the Rossby number, the bottom-heaviness of the heating rate and the time over which the heating acts (here given by the integration time). For the high Rossby number storm, doubling of the Rossby number to $\epsilon = 0.8$ leads to a surface PV anomaly that is about 5 times larger (not shown). This sensitive dependence of the PV asymmetry on the Rossby number and the bottom-heaviness of the heating profile explains the differences found between the PV structure of the winter and summer DRV example discussed in Kohl and O'Gorman (2022). In that case, the winter storm was found to be more asymmetric in terms of the magnitude of positive versus negative PV anomalies (no clear negative PV identifiable) because it was a stronger storm, implying a higher Rossby number, with a more bottom-heavy diabatic heating profile.

5. Conclusions

Finite amplitude effects in DRVs were explored in simulations of moist macroturbulence using the QG and primitive equations, and an attempt was made at synthesis in the form of a toy model of the vertical structure of PV.

Moist QG simulations with a reduced stability parametrization transition from a state of wavy jets interspersed with vortices to a vortex dominated state (DRV world) as latent heating is increased. PV budget analysis revealed that the vortices in the strong latent heating regime are DRVs with diabatic generation dominating over meridional PV advection. The solutions are maintained by a balance between mean zonal advection, nonlinear advection and diabatic generation. This is very similar to the balances maintaining the small-amplitude DRV mode from theory, with the additional effect of nonlinear advection which leads to poleward self advection. DRV world begins to emerge at about $r = 0.4$, which is similar to the condition of $r < 0.38$ for DRV modes to exist on an infinite domain (Kohl and O'Gorman 2024). One piece of evidence that DRV world is starting to emerge near $r = 0.4$ is that simulations run without radiative damping fail to equilibrate for $r \lesssim 0.4$ due to explosive growth of a single vortex in the domain. We also quantified the transition to DRV world using a moist growth-rate metric that measures collocation of PV anomalies with diabatic PV generation of the same sign, and this showed a rapid pickup near $r = 0.4$. It would be interesting to generalize and test this metric for storms in more realistic simulations and observations in future work.

Multilevel simulations of the moist primitive equations in a doubly periodic configuration were run for low, intermediate (closest to Earth-like conditions) and high Rossby number regimes while keeping latent heating strong. The simulations show that changes in the Rossby number cause important changes in the overall macroturbulent flow and the PV structure of strong diabatic storms. At low Rossby number the zonal flow becomes disrupted by isolated vorticity dipoles which continously spawned and self-advected poleward. The vertical velocity field breaks up into isolated maxima with a strong asymmetry between upward and downward motion. At high Rossby number the flow maintains a wave-like structure in the upper troposphere, and there are a mix of DRV-like storms and frontal features such that there is not a pure DRV world. The storms primarily propagate eastward although still with some weaker poleward propagation. In the intermediate Rossby number regime, rapidly poleward propagating vortices emerged as in the low

Rossby number regime. However, the flow also retained some frontal features that were observed in the high Rossby number regime. We conclude from this that the transition to DRV world with decreasing Rossby number appears to be gradual rather than abrupt. While the PV structure of strong diabatic storms in the low and intermediate Rossby number simulations resembles that of the QG DRV storms and DRV modes, the PV structure of storms in the high Rossby number simulations are more asymmetric and bottom confined and resembled that of DRVs observed in the current climate. We conclude that higher order terms in the PV dynamics beyond QG play an important role in setting the structure of storms, their propagation, and the extent to which the flow is dominated by DRVs.

Finite amplitude effects beyond the small-amplitude QG DRV theory were further explored within a simple toy model of the moist thermodynamic and PV equations in a single ascending column. The toy model was solved for a low, intermediate and a high Rossby number and found to reproduce much of the variety of storm structure found in the moist primitive equation simulations. For low Rossby numbers the diabatic PV tendency behaves like the vertical gradient of the latent heating profile (cf. Eq. 31). If the profile is symmetric this will lead to generation of positive and negative PV anomalies of equal magnitude, as was found for DRV storms in QG simulations and primitive equation simulations at small Rossby number. When the Rossby number is increased, the PV tendency is proportional to the product of the absolute vorticity and the heating rate - which amplifies the generation of positive PV anomalies but weakens the generation of negative PV anomalies, leading to a nonlinear feedback as the PV anomalies evolve. This leads to the low level positive PV anomaly being stronger than the negative PV anomaly aloft as was found in moist primitive equation simulations at intermediate and high Rossby numbers. In particular, it was found that when a strong Rossby number is coupled with a bottom heavy heating profile, which favors larger values of positive PV generation, this can lead to a feedback which rapidly generates strong low level PV anomalies with much smaller upper level negative anomaly - as is often found for DRVs observed in the current climate (e.g. Wernli et al. 2002, Kohl and O'Gorman 2022). Strong sensitivity of the asymmetry of the magnitude of negative versus positive PV anomalies was found to the degree of bottom heaviness of the heating rate and the magnitude of the Rossby number. Future work could investigate this sensitive dependence by looking at a variety of realistic storm systems and relating the vertical profile of heating rates to the magnitude of the PV anomalies.

Given that a negative PV anomaly is required for diabatic growth and poleward self-advection, the results lead us to the following speculation. In the current climate, where heating rates are more bottom heavy, diabatic generation leads to the rapid genesis of low level positive PV anomalies. The negative PV anomaly is quickly eroded away (or at least does not grow as quickly as the positive PV anomaly) limiting diabatic growth and poleward self advection. Meanwhile the diabatically generated positive PV anomaly has become sufficiently large in amplitude to be able to undergo nonlinear interaction with upper level PV anomalies in a later secondary growth process (Wernli et al. 2002).

The Rossby number in our simulations is given by $\epsilon = U/f_0 L_D = U/NH$ where U/H should be interpreted as the mean-state zonal wind shear (rather than, say, the local wind shear in a storm). Hence, smaller Rossby numbers could be achieved by weaker mean zonal shear or stronger static stability N, both of which could occur at least regionally in a warming midlatitude climate. Future work could investigate the extent to which there is a transition to a more vortex dominated flow (or even a full DRV world) in GCMs in warm and moist climates when the Rossby number is low, e.g. by varying the strength of the midlatitude jet. This would also include the β effect which was not considered in the primitive equation simulations described here, and it could confirm whether the tendency for a more vortex dominated flow to occur at low Rossby number and with strong latent heating holds in models with a more realistic representation of moist physics.

Acknowledgments. We acknowledge helpful discussions with Santiago Benavides, Andre da Silva, Minmin Fu, Martín Vélez-Pardo, Stephan Pfahl, Kerry Emanuel, and Glenn Flierl. We are grateful to Keaton Burns for help with the solver Dedalus which is available at https://dedalus-project.org/. We acknowledge support from NSF AGS 2031472 and the mTerra Catalyst Fund.

Data availability statement. Model code for the moist QG and moist primitive equation simulations is available on github (`https://github.com/matthieukohl/DRV_World_Paper`).

APPENDIX A

Comparison of two-layer QG models with and without a prognostic moisture variable

To make a closer comparison between moist QG models relying on a reduced static stability without prognostic moisture following Emanuel et al. (1987) and used in the present paper, and moist QG models with prognostic moisture variables following Lapeyre and Held (2004), we compare diagnostics focusing on the transition threshold from wave to vortex regime, the barotropic and baroclinic energy spectra, and the skewness of the vorticity field. This comparison is not exhaustive, and future work comparing the two parametrizations is needed. We compare our simulations primarily to the original paper of Lapeyre and Held (2004), as the super criticality value chosen is identical, and we also compare to Brown et al. (2023).

a. Transition Threshold to a Vortex regime

The key control parameter in our simulations is the static stability reduction parameter r which is related to the key control parameter μ_{sat} in Lapeyre and Held (2004) through the relation

$$r = \frac{1-\mathcal{L}}{1+C\mathcal{L}} = \frac{1}{\mu_{sat}}, \tag{A1}$$

where we have used Eq. 11 in Lapeyre and Held (2004) which holds for saturated air, and the definition of $\mu_{sat} = (1+C\mathcal{L})/(1-\mathcal{L})$. Here, $\mathcal{L}$ is a non dimensional measure of the strength of latent heating, and C is a non dimensional proportionality constant that determines how much the saturation humidity increases with temperature. Increases in latent heating $\mathcal{L}$ thus lead to increases in μ_{sat} and decreases in the static stability reduction parameter r.

Lapeyre and Held (2004) observed a regime transition towards a vortex dominated flow for values of $\mu_{sat} > 2.5$ as evidenced by an explosive energy increase in their simulations (see their Fig. 2a) and a marked jump in skewness in the vorticity field of the lower layer (see their Fig. 11b). This would correspond to the parameter regime $r < 0.4$ in our simulations which is exactly when a vortex world transition has been observed for our moist model with reduced stability parametrization. We note that an explosive energy increase has also been found for our simulations below $r < 0.4$ to the point that a radiative damping was required to stabilize the simulations. Such a damping was not required in the simulations of Lapeyre and Held (2004), and it is possible that this is a consequence of having a conserved moisture variable which limits the energetic input from latent heating. We note however that Lapeyre and Held (2004) only ran simulations up to roughly $\mu_{sat} = 4$ (or equivalently down to $r = 0.25$), which is only slightly below the vortex transition threshold, whereas simulations down to $r = 0.01$ have been performed in this paper. Given the rapid energy increase found by Lapeyre and Held (2004) with μ_{sat} (see their Fig. 2a), it is possible that simulations with stronger latent heating would also blow up in their model.

Overall, the main result of this section is that both our simulations with reduced stability parametrization and the simulations of Lapeyre and Held (2004) with explicit moisture variable agree on the transition point towards a vortex dominated flow: $r < 0.4$ which corresponds to $\mu_{sat} > 2.5$. This is also close to the threshold of $r < 0.38$ for a DRV mode to exist on an infinite domain (Kohl and O'Gorman 2022).

b. Energy Spectra

Fig. A1 shows the time-averaged barotropic and baroclinic energy spectra for the moist QG simulations at $r = 1$ (dry simulation) and $r = 0.3$ (moist simulation in the vortex regime).

A few key changes in the spectra can be observed going from dry to moist simulations. The barotropic and baroclinic energy increases, the peak of the barotropic energy spectrum shifts to larger scales, and the baroclinic energy spectrum broadens, such that its centroid shifts to smaller scales (not shown). As a result, while the peak of the barotropic and baroclinic energy occur at roughly the same wavenumber for the dry simulations, the spectra separate for the moist simulations. At large wavenumbers, the spectra of both dry and moist simulations follow a k^{-3} power law. These results are in good qualitative agreement with the results of Brown et al. (2023) (their Fig. 4). Even

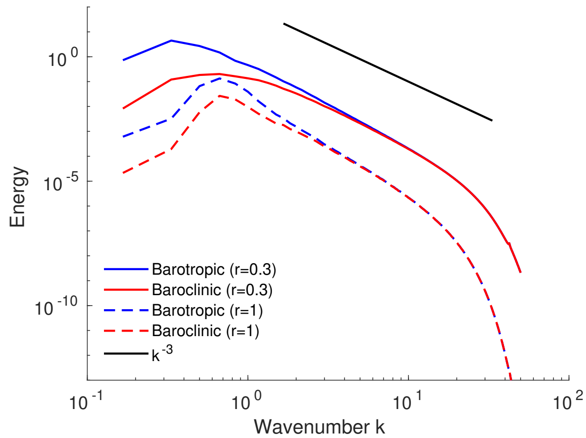

FIG. A1. Barotropic (blue) and baroclinic (red) energy spectra for the moist QG simulations with radiative damping of $\alpha = 0.15$ for a reduction factor $r = 1$ (dry simulation; dashed lines) and $r = 0.3$ (moist simulation in the vortex regime; solid lines).

though we focus only on a dry simulation and a moist simulation in the vortex regime, we note that the changes described before happen gradually as latent heating is increased without abrupt transition (not shown).

In the vortex regime of Lapeyre and Held (2004) at $\mu_{sat} = 3.14$ ($r = 0.32$), their upper-layer and lower-layer energy spectra had no discernible peak and increased all the way to the smallest wavenumber with flattening spectral slope (their Fig. 6b), unlike what is found for our barotropic energy spectrum which decreases at small wavenumbers (Fig. A1). It is possible that their simulations experienced more of an inverse cascade which could explain why their vortices, unlike ours, barotropized despite the baroclinic forcing from latent heating.

c. Cyclone/Anticyclone Asymmetry

Finally, we plot the skewness of the relative vorticity in the top and bottom layers as a measure of the cyclone/anticyclone asymmetry produced by the simulations (Fig. A2). As the reduction factor r is decreased, the relative vorticity in both layers becomes more skewed with a weak preference for anticyclones in the top layer and a stronger preference for cyclones in the bottom layer. These results are consistent with was found in Lapeyre and Held (2004). However, their simulations showed a rather abrupt increase in the skewness of the lower layer vorticity as the vortex regime was approached which we do not find in our simulations (see their Fig. 11b). In this regime, their

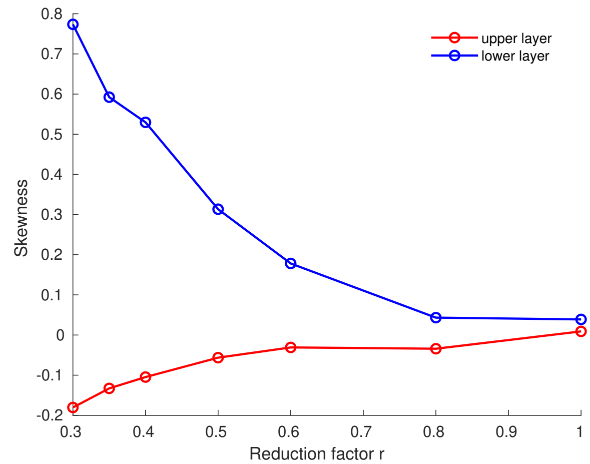

FIG. A2. Skewness of the relative vorticity in the top (red) and bottom (blue) layers as a function of the reduction factor r. All simulations were run with a radiative damping of $\alpha = 0.15$. Averages were taken between $t = 100 - 250$.

skewness in the lower layer is almost an order of magnitude larger than what we find. Further work is required to understand these differences, and how they are related to the tendency for vortices to barotropize in the simulations Lapeyre and Held (2004) but not in ours.

APPENDIX B

Vertical velocity asymmetry in the moist QG simulation

As discussed in section 2b, the moist QG simulation at $r = 0.01$ has a very high vertical velocity asymmetry parameter of $\lambda = 0.94$ as compared to $\lambda = 0.73$ for an idealized GCM simulation at $r = 0.01$ in O'Gorman et al. (2018). The effective wavenumber of the w-spectrum, as defined in Kohl and O'Gorman (2024), is much larger in the QG simulations compared to the idealized GCM simulation ($k = 6.1$ vs. $k = 1.7$). Given these k values and $r = 0.01$, the toy model for λ of Kohl and O'Gorman 2024 predicts a higher value of $\lambda = 0.84$ for the QG simulation compared to a prediction of $\lambda = 0.75$ for the GCM simulation. The toy model underestimates λ in the QG simulation even given the high k, which is likely a result of the fact the toy model is 1D whereas the vertical velocity field in the QG simulation has a more 2D structure (vortices) compared to the 1D structure (fronts) in the idealized GCM.

To investigate further, we expand the toy model of Kohl and O'Gorman 2024 slightly to two dimensions by solving

$$\nabla^2(r(w)w) - w = \sin(kx)\sin(ky) \tag{B1}$$

numerically for a given wavenumber k and reduction factor r on a domain of length $L_x = L_y = 2\pi/k$ using 300 evenly spaced grid points in each direction. The solution technique follows the method outlined in Kohl and O'Gorman 2024. This 2D version of the toy model predicts a value of the asymmetry of $\lambda = 0.92$ for the QG simulation at $r = 0.01$ which is in good agreement with the simulated value of $\lambda = 0.94$. As discussed in Kohl and O'Gorman 2024, the asymmetry is larger for 2D flow features because of the greater contribution from the Laplacian term in that case.

APPENDIX C

PV equation for the primitive-equation model

Eqs. (11-14) can be combined into an equation for the PV Q (Vallis 2017, his Eq. 4.96)

$$\frac{DQ}{Dt} = (f_0+\zeta)\dot{\theta}_z - v_z\dot{\theta}_x + u_z\dot{\theta}_y, \tag{C1}$$

where

$$Q = (f_0+\zeta)\theta_z - v_z\theta_x + u_z\theta_y, \tag{C2}$$

$$\dot{\theta} = (1-r)w\theta_z, \tag{C3}$$

$$\theta_z = \bar{\theta}_z + \theta_z', \tag{C4}$$

$$\frac{D}{Dt} = \partial_t + u\partial_x + v\partial_y + w\partial_z, \tag{C5}$$

$\bar{\theta}_z$ is a background stratification, and we have ignored the drag, relaxation and hyperdiffusion terms in Eq. (C1). Nondimensionalizing the vertical potential temperature gradients as $\theta_z' \sim \theta_0 f_0 U L_D/gH^2$, $\bar{\theta}_z \sim \theta_0 N^2/g$, the PV like $Q \sim f_0\bar{\theta}_z = f_0\theta_0 N^2/g$ and the rest of the variables with scales as outlined in section (3), we obtain the nondimensional PV equation

$$\frac{DQ}{Dt} = \epsilon(1+\epsilon\zeta)\dot{\theta}_z - \epsilon^2 v_z\dot{\theta}_x + \epsilon^2 u_z\dot{\theta}_y, \tag{C6}$$

where

$$Q = (1+\epsilon\zeta)\theta_z - \epsilon^2 v_z\theta_x + \epsilon^2 u_z\theta_y, \tag{C7}$$

$$\dot{\theta} = (1-r)w\theta_z, \tag{C8}$$

$$\theta_z = \bar{\theta}_z + \epsilon\theta'_z, \tag{C9}$$

$$\frac{D}{Dt} = \partial_t + u\partial_x + v\partial_y + \epsilon w\partial_z \tag{C10}$$

and all variables are now nondimensional. Eq. (C7) corresponds to Eq. (30) used for the PV in section (3), where in that section we use a background stratification equal to the reference state such that $\theta_z = 1+\epsilon\theta'_z$. The first term on the rhs of Eq. (C6) corresponds to Eq. (31) used for the PV tendency from latent heating in section (3).

APPENDIX D

Derivation of the governing equations for the 1-D toy model of vertical PV structure

If we place ourselves at the location of the heating maximum $\dot{\theta}_x = \dot{\theta}_y = 0$, neglect all horizontal transport of PV, and neglect the higher order vertical shear terms in the PV, then Eqs. (C6) and (C7) simplify to

$$\partial_t Q + \epsilon w Q_z = \epsilon(1+\epsilon\zeta)\dot{\theta}_z \tag{D1}$$

$$Q = (1+\epsilon\zeta)\theta_z, \tag{D2}$$

which we can rewrite as

$$\partial_t Q = \epsilon\frac{Q\dot{\theta}_z}{\bar{\theta}_z + \epsilon\theta'_z} - \epsilon w Q_z, \tag{D3}$$

which is the form of the PV equation (Eq. 33) used in the simple 1D toy-model in section (4).

The thermodynamic equation in the simple 1-D toy model (Eq. 32) is derived similarly to Eq. (26) but neglecting horizontal advection of perturbation θ' and reference theta (the v term), neglecting hyperdiffusion and radiative relaxation, and using $\bar{\theta}$ in place of θ_r.

References

Abbott, T. H., and P. A. O'Gorman, 2024: Impact of precipitation mass sinks on midlatitude storms in idealized simulations across a wide range of climates. *Weather and Climate Dynamics*, https://doi.org/10.5194/wcd-5-17-2024.

Ahmadi-Givi, F., G. C. Graig, and R. S. Plant, 2004: The dynamics of a midlatitude cyclone with very strong latent-heat release. *Quart. J. Roy. Meteor. Soc.*, **130**, 295–323, https://doi.org/10.1256/qj.02.226.

Bembenek, E., D. N. Straub, and T. M. Merlis, 2020: Effects of moisture in a two-layer model of the midlatitude jet stream. *J. Atmos. Sci.*, **77**, 131–147, https://doi.org/10.1175/JAS-D-19-0021.1.

Boettcher, M., and H. Wernli, 2013: A 10-yr climatology of diabatic rossby waves in the northern hemisphere. *Mon. Wea. Rev.*, **141**, 1139–1154, https://doi.org/10.1175/MWR-D-12-00012.1.

Boettcher, M., and H. Wernli, 2015: Diabatic Rossby waves in the Southern Hemisphere. *Quarterly Journal of the Royal Meteorological Society*, **141**, 3106–3117, https://doi.org/10.1002/qj.2595.

Brown, M. L., O. Pauluis, and E. P. Gerber, 2023: Scaling for Saturated Moist Quasigeostrophic Turbulence. *Journal of the Atmospheric Sciences*, https://doi.org/10.1175/JAS-D-22-0215.1.

Burns, K. J., G. M. Vasil, J. S. Oishi, D. Lecoanet, and B. P. Brown, 2020: Dedalus: A flexible framework for numerical simulations with spectral methods. *Physical Review Research*, **2**, 023 068, https://doi.org/10.1103/PhysRevResearch.2.023068.

Charney, J. G., 1947: The dynamics of long waves in a baroclinic westerly current. *J. Atmos. Sci.*, **4**, 136–162, https://doi.org/10.1175/1520-0469(1947)004⟨0136:tdolwi⟩2.0.co;2.

Davis, C. A., and K. A. Emanuel, 1991: Potential vorticity diagnostics of cyclogenesis. *Monthly Weather Review*, **119**, 1929–1953, https://doi.org/10.1175/1520-0493(1991)119⟨1929:PVDOC⟩2.0.CO;2.

Eady, E. T., 1949: Long Waves and Cyclone Waves. *Tellus*, **1**, 33–52, https://doi.org/10.3402/tellusa.v1i3.8507.

Emanuel, K. A., M. Fantini, and A. J. Thorpe, 1987: Baroclinic instability in an environment of small stability to slantwise moist convection. Part I: two-dimensional models. *J. Atmos. Sci.*, **44**, 1559–1573, https://doi.org/10.1175/1520-0469(1987)044⟨1559:BIIAEO⟩2.0.CO;2.

Fantini, M., 1995: Moist Eady waves in a quasigeostrophic three-dimensional model. *J. Atmos. Sci.*, **52**, 2473–2485.

Hogg, N., and H. Stommel, 1985: The heton, an elementary interaction between discrete baroclinic geostrophic vortices, and its implications concerning eddy heat-flow. *Proceedings of the Royal Society of London. A. Mathematical and Physical Sciences*, **397**, 1–20, https://doi.org/10.1098/rspa.1985.0001.

Kohl, M., and P. A. O'Gorman, 2022: The Diabatic Rossby Vortex: Growth Rate, Length Scale and the Wave-Vortex Transition. *J. Atmos. Sci.*, **79**, 2739–2755.

Kohl, M., and P. A. O'Gorman, 2024: Asymmetry of the Distribution of Vertical Velocities of the Extratropical Atmosphere in Theory, Models, and Reanalysis. *Journal of the Atmospheric Sciences*, **81**, 545–559, https://doi.org/10.1175/JAS-D-23-0128.1.

Lambaerts, J., G. Lapeyre, and V. Zeitlin, 2011: Moist versus dry barotropic instability in a shallow-water model of the atmosphere with moist convection. *Journal of the Atmospheric Sciences*, **68**, 1234–1252, https://doi.org/10.1175/2011JAS3540.1.

Lambaerts, J., G. Lapeyre, and V. Zeitlin, 2012: Moist versus dry baroclinic instability in a simplified two-layer atmospheric model with condensation and latent heat release. *J. Atmos. Sci.*, **69**, 1405–1426, https://doi.org/10.1175/JAS-D-11-0205.1.

Lapeyre, G., and I. M. Held, 2004: The Role of Moisture in the Dynamics and Energetics of Turbulent Baroclinic Eddies. *Journal of the Atmospheric Sciences*, **61**, 1693–1710, https://doi.org/10.1175/1520-0469(2004)061⟨1693:tromit⟩2.0.co;2.

Lutsko, N. J., J. Martinez-Claros, and D. D. B. Koll, 2024: Atmospheric Moisture Decreases Mid-Latitude Eddy Kinetic Energy. *Journal of the Atmospheric Sciences*, **81**, 1817–1832, https://doi.org/10.1175/jas-d-23-0226.1.

Montgomery, M. T., and B. F. Farrell, 1991: Moist surface frontogenesis associated with interior potential vorticity anomalies in a semigeostrophic model. *J. Atmos. Sci.*, **48**, 343–368, https://doi.org/10.1175/1520-0469(1991)048⟨0343:msfawi⟩2.0.co;2.

Montgomery, M. T., and B. F. Farrell, 1992: Polar low dynamics. *J. Atmos. Sci.*, **49**, 2484–2505, https://doi.org/10.1175/1520-0469(1992)049⟨2484:PLD⟩2.0.CO;2.

Moore, R. W., and M. T. Montgomery, 2004: Reexamining the dynamics of short-scale, diabatic rossby waves and their role in midlatitude moist cyclogenesis. *J. Atmos. Sci.*, **61**, 754–768, https://doi.org/10.1175/1520-0469(2004)061⟨0754:RTDOSD⟩2.0.CO;2.

Moore, R. W., and M. T. Montgomery, 2005: Analysis of an idealized, three-dimensional diabatic Rossby vortex: A coherent structure of the moist baroclinic atmosphere. *J. Atmos. Sci.*, **62**, 2703–2725, https://doi.org/10.1175/JAS3472.1.

Moore, R. W., M. T. Montgomery, and H. C. Davies, 2008: The integral role of a diabatic rossby vortex in a heavy snowfall event. *Mon. Wea. Rev.*, **136**, 1878–1897, https://doi.org/10.1175/2007MWR2257.1.

O'Gorman, P. A., T. M. Merlis, and M. S. Singh, 2018: Increase in the skewness of extratropical vertical velocities with climate warming: fully nonlinear simulations versus moist baroclinic instability. *Quart. J. Roy. Meteor. Soc.*, **144**, 208–217, https://doi.org/10.1002/qj.3195.

O'Gorman, P. A., 2011: The effective static stability experienced by eddies in a moist atmosphere. *J. Atmos. Sci.*, **68**, 75–90, https://doi.org/10.1175/2010JAS3537.1.

Phillips, N., 1954: Energy Transformations and Meridional Circulations associated with simple Baroclinic Waves in a two-level, Quasi-geostrophic Model. *Tellus*, **6**, 273–286, https://doi.org/10.1111/j.2153-3490.1954.tb01123.x.

Schubert, W., and B. Alworth, 1987: Evolution of potential vorticity in tropical cyclones. *Quarterly Journal of the Royal Meteorological Society*, **113**, 147–162.

Smith, L. M., and S. N. Stechmann, 2017: Precipitating quasigeostrophic equations and potential vorticity inversion with phase changes. *Journal of the Atmospheric Sciences*, **74**, 3285–3303, https://doi.org/10.1175/JAS-D-17-0023.1.

Vallis, G. K., 2017: *Atmospheric and oceanic fluid dynamics: Fundamentals and large-scale circulation, second edition*. Cambridge University Press, https://doi.org/10.1017/9781107588417.

Wernli, H., S. Dirren, M. A. Liniger, and M. Zillig, 2002: Dynamical aspects of the life cycle of the winter storm 'Lothar' (26-26 December 1999). *Quart. J. Roy. Meteor. Soc.*, **128**, 405–429, https://doi.org/10.1256/003590002321042036.

Zurita-Gotor, P., 2005: Updraft/downdraft constraints for moist baroclinic modes and their implications for the short-wave cutoff and maximum growth rate. *J. Atmos. Sci.*, **62**, 4450–4458, https://doi.org/10.1175/JAS3630.1.